

On the internal blast loading of submerged floating tunnels in concrete with circular and rectangular cross-sections

Martin Kristoffersen^{a,*}, Arianna Minoretti^b, Tore Børvik^a

^a*Structural Impact Laboratory (SIMLab), Department of Structural Engineering,
Norwegian University of Science and Technology (NTNU),
Rich. Birkelands vei 1A, NO-7491 Trondheim, Norway*

^b*Norwegian Public Roads Administration, Abels gate 5, NO-7030 Trondheim, Norway*

Abstract

The Norwegian Public Roads Administration has initiated a large research project on a potential ferry-free coastal highway route E39 on the west coast of Norway. For the wide and deep fjords, a submerged floating tunnel (SFT) in reinforced concrete has been suggested as a possible solution. A potential hazard for such a structure is internal blast loading, which can be devastating to its structural integrity. To assess the blast performance of concrete structures, a shock tube has been used to generate blast loading against concrete slabs with and without reinforcement. The shock tube tests were filmed with high-speed cameras, and digital image correlation was used to measure the out-of-plane deformations. A finite element model using input from material tests was set up in ABAQUS/Explicit to recreate the slab experiments. Based on the models validated by the shock tube experiments, full-scale numerical simulations of blast loaded SFTs with circular and rectangular cross-sections were run. The results were used to assess the qualitative performance of each cross-section geometry with respect to blast loading, where the circular cross-section indicated a superior behaviour.

Keywords: mechanical testing, finite element analysis, damage assessment, explosions, structural integrity

1. Introduction

The Norwegian Public Roads Administration (NPRA) conducts a large research project aimed at replacing ferries with fixed connections along the E39 coastal highway route from Trondheim

*Corresponding author, tel.: +47-73-59-46-66; fax: +47-73-59-47-01

Email address: martin.kristoffersen@ntnu.no (Martin Kristoffersen)

to Kristiansand [1]. Part of this route involves crossing wide and deep fjords, where one of the suggested crossing alternatives is a submerged floating tunnel (SFT) built in concrete (see e.g. the work by Tveit [2]). The concept has been judged viable in a feasibility study [3]. In addition to the typical design challenges exemplified in the work by Jakobsen [4], the SFT concept involves additional challenges. Fluid-structure interaction (FSI) is one of them, and this topic has been studied for this type of structure [5, 6]. Leira [7] has presented simplified calculations for slow-drift excitation. Even fluid-vehicle-tunnel interaction has received attention [8], and scaled models have been used to verify a theoretical description of SFT motion in waves [9]. Xiang et al. [10] investigated hydrodynamic loads due to passing ships, while impact from ships has been investigated as well [11, 12]. Seismic loads are another important aspect [13, 14], although of relatively minor significance in Norway. Other major concerns regarding an SFT are internal blast loading and fire from accidents involving tankers transporting dangerous cargo, like liquid natural gas or gasoline, or from a potential terrorist attack.

Concrete exposed to blast loading has been extensively studied through several approaches – experimentally [15, 16], numerically [17, 18], analytically/empirically [19, 20], or any combination of these [21–23]. SFTs have yet to be thoroughly analysed for this type of loading, although a preliminary study was presented in [24]. Other civil infrastructures in concrete relevant to the case presented herein have also been studied. Dam structures subjected to close-in underwater blast loading have been examined numerically by Zhao et al. [25], who found that detonations inside the dam openings cause far greater damage than detonations outside. Colombo et al. [26] used a shock tube to study the performance of a protective layer intended for internal use in tunnels through soil. Foglar and Kovar [27] studied blast loaded bridge decks using both normal reinforced concrete and reinforced concrete with fibres, where the fibres were shown to reduce the volume of debris (and hence the crater) and change the behaviour from brittle to more ductile. A typical box-shaped bridge girder exposed to blast loading was simulated by Shiravand and Parvanehro [28], who found that the anchor zones of pre-stressed tendons were vulnerable parts. Placing the charge inside a box bridge girder produced more damage due to the confinement [29], a result which was also obtained experimentally for concrete pipes [30]. Using numerical simulations, it was found that protective linings may mitigate blast load effects inside rock tunnels [31].

Through numerical simulations using ABAQUS/Explicit [32], this study evaluates the relative

performance between two different cross-sectional designs of an SFT – a circular and a rectangular – with respect to blast loading. Due to practical and financial obstacles, full-scale testing is not an option in this case, and one has to rely on the finite element method (FEM). To provide some grounds for making reasonable predictions, material tests are required. Quasi-static compression tests were performed on standard 100 mm concrete cubes, and on 50 mm concrete cubes cut from the standard 100 mm specimens. The force and deformations were measured continuously throughout the testing of the 50 mm specimens, and a constitutive relation was calibrated to the test data. The same procedure was carried out for the 2.6 mm diameter steel reinforcement bars by using tension tests instead of compression tests. Four concrete slabs (two with reinforcement and two without) cast from the tested concrete mix were loaded in a shock tube [33, 34] and filmed at 24 000 frames per second using high-speed cameras. Shock tubes are considered reliable tools for assessing the blast performance of concrete structures [26, 35, 36]. A 3D digital image correlation (DIC) procedure [37] applicable both to small [34] and large [38] deformations was used to measure the out-of-plane deformation of the slabs tested in the shock tube. The shock tube tests were then employed as validation cases for finite element models using the calibrated constitutive relations for the concrete and the steel reinforcement. The slabs were discretised using 8-node linear brick elements with reduced integration. The numerical results showed good correlation with the experimental data in terms of out-of-plane deformation and damage pattern, for both the plain and reinforced concrete slabs.

Finally, the validated model was used to make predictions about the blast performance of circular and rectangular cross-sections developed for the possible crossings of the Bjørnafjord and Digernessundet [3, 39]. Blast loads were applied to the relevant surfaces by using the CONWEP module available in ABAQUS/Explicit [32]. These blast loads are based on the experimental data obtained by Kingery and Bulmash [40]. The study aims to investigate what is possible to obtain without invoking complicated numerical setups like fully-coupled Eulerian-Lagrangian approaches, since the fluid-structure interaction (aside from reflections/confinement) in this problem is considered small. Different charge sizes were placed in the middle of the driving lane closest to the outer wall for both cross-sections. The charge sizes were 10 kg, 100 kg and 500 kg TNT placed 1.0 m above the driving lanes. The numerical simulations indicated that the circular cross-section is preferable to the rectangular cross-section with respect to blast loading.

2. Concrete

2.1. Material testing

The concrete mix used herein had a water to cement ratio of 0.62 (8.0 % of the weight was water and 12.9 % cement). Further, 50.1 % of the weight was aggregate sized 0-8 mm, and 29.0 % was sized 8-16 mm. Quasi-static compression tests on 100 mm cubes were conducted after 2, 7, 14, 28, 49 and 85 days of curing and the results are shown in Fig. 1(a). A fully automated load controlled Toni Tech 3000 kN apparatus increased the load at a rate of 0.8 MPa/s until a peak was detected. The estimated cube compressive strength \hat{f}_c after D_t days is [41]

$$\hat{f}_c(D_t) = \bar{f}_c \cdot \exp\left(s \cdot \left[1 - \sqrt{\frac{28}{D_t}}\right]\right) \quad (1)$$

Here, s depends on the type of cement, and \bar{f}_c is the average strength after 28 days of curing. 20 cube compression tests after 28 days gave $\bar{f}_c = 46.3 \pm 0.8$ MPa (see Fig. 1(b)).

Additionally, three concrete cubes with 50 mm sides were tested quasi-statically in an Instron 5985 250 kN testing rig (see Fig. 2(a)), at a deformation rate of 0.5 mm/min. The cube size was reduced to keep the loads within the limits of the rig capacity to study size effects, and to obtain engineering stress-strain curves for calibration of the material model. Thus, the smaller cubes were used as a component for inverse modelling of the material model in Section 2.2. The 50 mm cubes were cut from 100 mm cubes, and painted with a speckled pattern (top row of Fig. 3) for use with DIC. A load cell registered the force, while the finite element-based DIC software eCorr [37] synchronised with the force measurements was used to compute the strains. Each element in the

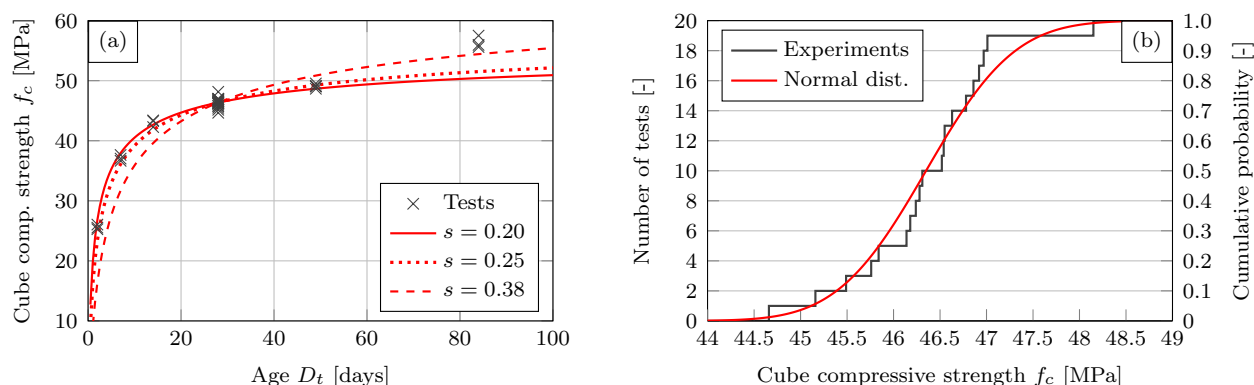


Fig. 1: Results from 100 mm cube compressive tests, where part (a) shows the cube compressive strength of the 100 mm cubes as a function of days of curing, and (b) the distribution of the 20 cubes tested 28 days after casting.

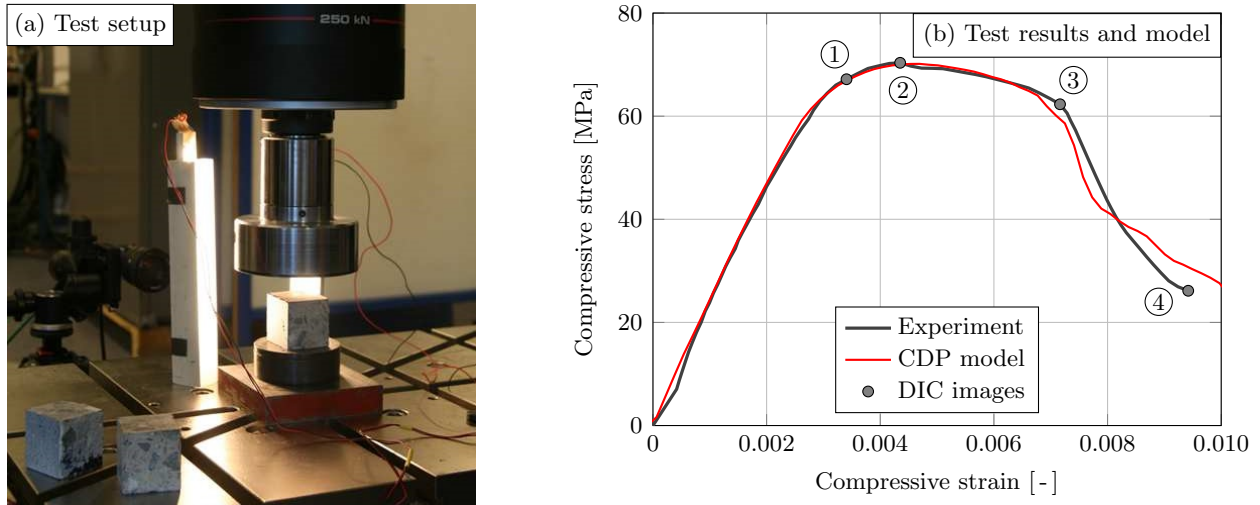


Fig. 2: Overview of concrete compression tests, where (a) shows the setup and (b) gives the results in terms of compressive engineering stress-engineering strain where the circled numbers correspond to the DIC images in Fig. 3.

105 structured quadrilateral Q4 mesh measured $50 \text{ pixels} \times 50 \text{ pixels}$. Note that too few pixels per element results in more noise, while too large elements are unable to capture finer nuances in the strain field [37]. The resulting compressive engineering stress-engineering strain curve is shown in Fig. 2(b).

By using DIC on the cubes directly, potential deformations in the rig are excluded. The cube
 110 compressive strength in the three tests was measured to 70.6 MPa, 68.1 MPa, and 78.1 MPa, where the stress-strain curve from the first of these is shown in Fig. 2(b). This curve was chosen for calibration of the material model because it was the middle value, and because it had the best post-peak DIC results. Some key points of the DIC analysis are illustrated in Fig. 3. As seen, the DIC analysis is able to pick up cracks before they are visible to the naked eye. The average
 115 value of the compressive strength was 72.3 MPa for the three 50 mm cubes, which is significantly higher than the 56.4 MPa obtained for the 100 mm cubes with the same curing conditions, i.e., 84 days submerged in water at room temperature, after which they were stored in a dry room for approximately one year. Any strength gain during this period is judged to be negligible since a relative humidity of 80% is required to prolong hydration [42]. Smaller cubes appear stronger due
 120 to the size effect, with a 22 % reduction when going from 50 mm cubes to 100 mm cubes – a result which is comparable with previous work [43, 44].

Cylinders measuring 100 mm in diameter and 200 mm in height were used in tensile splitting

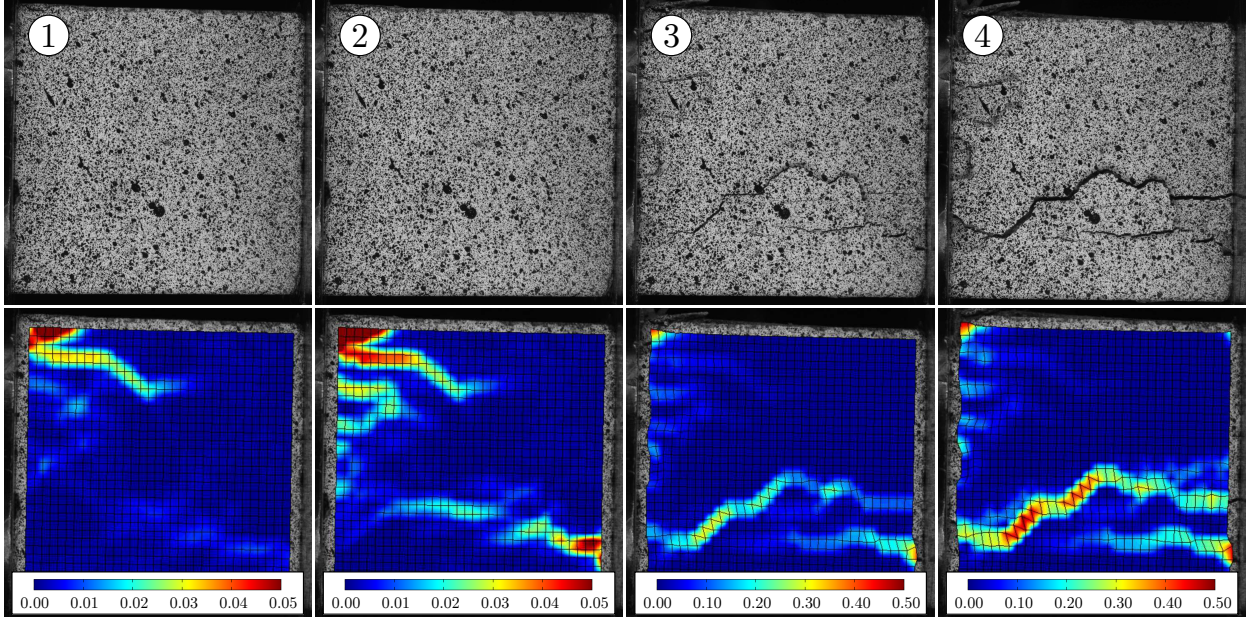


Fig. 3: DIC analysis showing the major principal strain on the surface of a concrete cube during compression (load direction is left to right), where the circled numbers correspond to specific points on the engineering stress-engineering strain curve in Fig. 2(b). Note the change of legend from the second to the third column.

(Brazilian) tests. The tensile strength and standard deviation from three tests were determined to 3.5 ± 0.34 MPa after 28 days of curing. The mass density ρ_c was measured to 2445 kg/m^3 .

125 2.2. Concrete damaged plasticity model

The concrete model used herein is the “Concrete damaged plasticity” model (CDP) as implemented in ABAQUS [32]. It is based on the work by Lubliner et al. [45], and by Lee and Fenves [46]. The model assumes an additive strain rate decomposition $\dot{\epsilon} = \dot{\epsilon}_{el} + \dot{\epsilon}_{pl}$, in which $\dot{\epsilon}$, $\dot{\epsilon}_{el}$ and $\dot{\epsilon}_{pl}$ are the total, elastic and plastic strain rate tensors, respectively. The strains ϵ are obtained by
 130 integration over the time t , $\epsilon = \int_0^t \dot{\epsilon} dt$ (valid for all strain quantities). The Cauchy stress tensor σ is expressed by

$$\sigma = (1 - d) \mathbf{D}_{0,el} : (\epsilon - \epsilon_{pl}) = \mathbf{D}_{el} : (\epsilon - \epsilon_{pl}) \quad (2)$$

where d is the scalar damage parameter, $\mathbf{D}_{0,el}$ is the undamaged elastic stiffness, and $\mathbf{D}_{el} = (1 - d) \mathbf{D}_{0,el}$ is the degraded elastic stiffness. Similarly, the effective stress tensor $\bar{\sigma}$ is scaled by $1 - d$ so that $\bar{\sigma} = \sigma / (1 - d)$. Here, $1 - d$ can be thought to represent the fraction of effective

135 load carrying area. The model is formulated in terms of the effective stress $\bar{\sigma}$ and the tensile and compressive equivalent plastic strains $\tilde{\epsilon}_{\text{pl}} = [\tilde{\epsilon}_{\text{pl},t} \quad \tilde{\epsilon}_{\text{pl},c}]^T$ where subscripts t and c refer to tensile and compressive, respectively. The equivalent plastic strain rates $\dot{\tilde{\epsilon}}_{\text{pl},t}$ and $\dot{\tilde{\epsilon}}_{\text{pl},c}$ are defined by

$$\dot{\tilde{\epsilon}}_{\text{pl}} = \begin{bmatrix} \dot{\tilde{\epsilon}}_{\text{pl},t} \\ \dot{\tilde{\epsilon}}_{\text{pl},c} \end{bmatrix} = \hat{\mathbf{h}} \hat{\dot{\epsilon}}_{\text{pl}} = \begin{bmatrix} h(\hat{\sigma}) & 0 & 0 \\ 0 & 0 & -(1-h(\hat{\sigma})) \end{bmatrix} \begin{bmatrix} \hat{\dot{\epsilon}}_{\text{pl},1} \\ \hat{\dot{\epsilon}}_{\text{pl},2} \\ \hat{\dot{\epsilon}}_{\text{pl},3} \end{bmatrix} \quad (3)$$

where $\hat{\dot{\epsilon}}_{\text{pl},1} \geq \hat{\dot{\epsilon}}_{\text{pl},2} \geq \hat{\dot{\epsilon}}_{\text{pl},3}$ are the ordered eigenvalues of the plastic strain rate tensor $\dot{\epsilon}_{\text{pl}}$. The function h depends on the eigenvalues $\hat{\sigma}_i$ (principal stresses) of the effective stress tensor $\bar{\sigma}$, i.e.,

$$h(\hat{\sigma}_i) = \frac{\sum_{i=1}^3 \langle \hat{\sigma}_i \rangle}{\sum_{i=1}^3 |\hat{\sigma}_i|} \quad (4)$$

140 The Macaulay bracket $\langle \bullet \rangle$ is defined as $\langle x \rangle = (x + |x|)/2$, meaning that Eq. (4) ranges from $h = 1$ when all the principal stresses are positive, to $h = 0$ when they are all negative. Thus, Eq. (3) gives $\dot{\tilde{\epsilon}}_{\text{pl},t} = \dot{\epsilon}_{\text{pl},11}$ for uniaxial tension and $\dot{\tilde{\epsilon}}_{\text{pl},c} = -\dot{\epsilon}_{\text{pl},11}$ for uniaxial compression.

ABAQUS [32] allows for different damage evolution in tension and compression, so the damage parameter d is decomposed into tensile and compressive parts,

$$1 - d = (1 - d_c) (1 - h(\hat{\sigma}) \cdot d_t) \quad (5)$$

145 Here it is assumed full stiffness recovery if the load changes from tension to compression (closure of microcracks), and no stiffness recovery if the load changes from compression to tension. The parameters d_t and d_c as functions of cracking and inelastic strains (respectively) are input as tabulated values in ABAQUS [32]. The equivalent plastic strains $\tilde{\epsilon}_{\text{pl},t}$ and $\tilde{\epsilon}_{\text{pl},c}$ are calculated from the cracking strain $\tilde{\epsilon}_{\text{ck},t}$ and the inelastic strain $\tilde{\epsilon}_{\text{in},c}$ as

$$\tilde{\epsilon}_{\text{pl},t} = \tilde{\epsilon}_{\text{ck},t} - \frac{d_t}{1 - d_t} \cdot \frac{\sigma_t}{E_c} \quad (6a)$$

$$\tilde{\epsilon}_{\text{pl},c} = \tilde{\epsilon}_{\text{in},c} - \frac{d_c}{1 - d_c} \cdot \frac{\sigma_c}{E_c} \quad (6b)$$

150 where E_c is in the initial undamaged Young's modulus of concrete, and σ_t and σ_c are the tensile and compressive cohesion stresses. If the stresses σ_t and/or σ_c become too large, e.g. due to erroneous

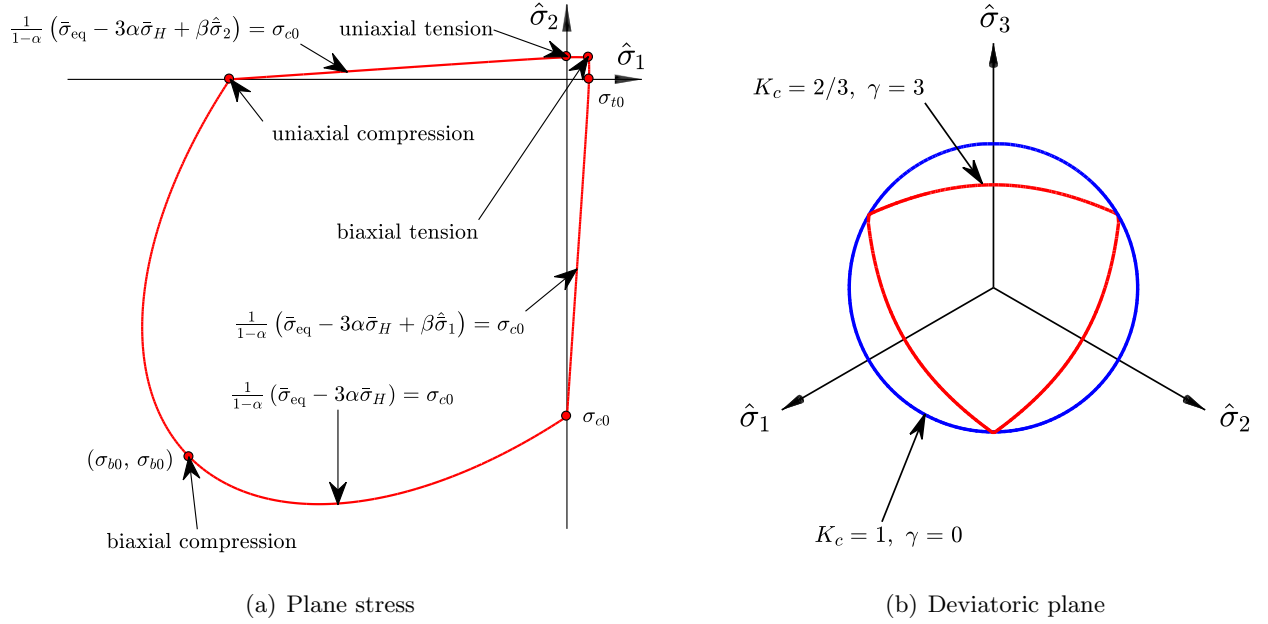


Fig. 4: Yield surface in (a) plane stress, and (b) in the deviatoric plane.

input or strain rate effects like discussed below, $\tilde{\varepsilon}_{pl,t}$ and $\tilde{\varepsilon}_{pl,c}$ might end up being not monotonically increasing (or even negative). This generates an error message in ABAQUS [32].

The yield function F , illustrated in Fig. 4, is also expressed in terms of the effective stress tensor $\bar{\boldsymbol{\sigma}}$ and the equivalent plastic strains $\tilde{\varepsilon}_{pl}$ as

$$F(\bar{\boldsymbol{\sigma}}, \tilde{\varepsilon}_{pl}) = \frac{1}{1-\alpha} [\bar{\sigma}_{eq} - 3\alpha\bar{\sigma}_H + \beta(\tilde{\varepsilon}_{pl})\langle\hat{\sigma}_1\rangle - \gamma\langle-\hat{\sigma}_1\rangle] - \bar{\sigma}_c(\tilde{\varepsilon}_{pl,c}) \quad (7)$$

Here, $\bar{\sigma}_{eq}$ is the equivalent von Mises stress of the effective stress tensor and $\bar{\sigma}_H$ is the effective hydrostatic stress, given as

$$\bar{\sigma}_{eq} = \sqrt{\frac{3}{2} \bar{\boldsymbol{\sigma}}^{dev} : \bar{\boldsymbol{\sigma}}^{dev}} \quad \bar{\sigma}_H = -\frac{1}{3} \bar{\boldsymbol{\sigma}} : \mathbf{I} \quad (8)$$

with $\bar{\boldsymbol{\sigma}}^{dev}$ being the deviatoric part of the effective stress tensor $\bar{\boldsymbol{\sigma}}$, and \mathbf{I} is the second order identity tensor. Further, $\hat{\sigma}_1$ is the largest principal stress of the effective stress tensor. This means that the function $\beta(\tilde{\varepsilon}_{pl})$ is active when $\hat{\sigma}_1 > 0$, and the parameter γ appears when $\hat{\sigma}_1 < 0$ (triaxial compression). For $\hat{\sigma}_1 = 0$ (biaxial compression) neither of these are active and α governs the yield function alone, thus reducing the yield function to the familiar Drucker-Prager yield function. The yield surface for plane stress conditions is shown in Fig. 4(a).

The parameter α in the yield function depends on the ratio of the initial biaxial compression strength σ_{b0} to the initial uniaxial compression strength σ_{c0} , i.e.,

$$\alpha = \frac{(\sigma_{b0}/\sigma_{c0}) - 1}{2(\sigma_{b0}/\sigma_{c0}) - 1} \quad (9)$$

The ratio σ_{b0}/σ_{c0} is assumed constant and given as input to the material model. The function $\beta(\tilde{\boldsymbol{\epsilon}}_{\text{pl}})$ is given by

$$\beta(\tilde{\boldsymbol{\epsilon}}_{\text{pl}}) = \frac{\bar{\sigma}_c(\tilde{\boldsymbol{\epsilon}}_{\text{pl},c})}{\bar{\sigma}_t(\tilde{\boldsymbol{\epsilon}}_{\text{pl},t})} (1 - \alpha) - (1 + \alpha) \quad (10)$$

in which $\bar{\sigma}_t = \sigma_t/(1 - d_t)$ and $\bar{\sigma}_c = \sigma_c/(1 - d_c)$ are the effective tensile and compressive cohesion stresses, respectively. Finally, γ is calculated from

$$\gamma = \frac{3(1 - K_c)}{2K_c - 1} \quad (11)$$

where K_c is the ratio (assumed constant) of the second stress invariant on the tensile meridian (Lode parameter $L = -1$) to that on the compressive meridian ($L = +1$). The Lode parameter L is defined by

$$L = \frac{2\hat{\sigma}_2 - \hat{\sigma}_1 - \hat{\sigma}_3}{\hat{\sigma}_1 - \hat{\sigma}_3} \quad (12)$$

The compressive meridian is the body of stress states satisfying $\hat{\sigma}_1 = \hat{\sigma}_2 > \hat{\sigma}_3$, and the tensile meridian satisfies the condition $\hat{\sigma}_1 > \hat{\sigma}_2 = \hat{\sigma}_3$, with $\hat{\sigma}_1 \geq \hat{\sigma}_2 \geq \hat{\sigma}_3$ being the ordered principal stresses of the effective stress tensor. K_c thus defines the yield surface shape in the deviatoric plane and is also required input to the material model. The effect of K_c on the yield surface is plotted in Fig. 4(b), which shows the yield surface in the deviatoric plane.

The plastic flow is governed by the Drucker-Prager hyperbolic function $G(\bar{\boldsymbol{\sigma}})$,

$$G(\bar{\boldsymbol{\sigma}}) = \sqrt{(\epsilon\sigma_{t0} \tan \psi)^2 + \bar{\sigma}_{\text{eq}}^2} - \bar{\sigma}_H \tan \psi \quad (13)$$

where σ_{t0} is the uniaxial tensile strength at failure (taken from the user specified tension stiffening data), ψ is the dilatation angle in the $\bar{\sigma}_H$ - $\bar{\sigma}_{\text{eq}}$ plane at high confining pressures (see Fig. 5), and ϵ

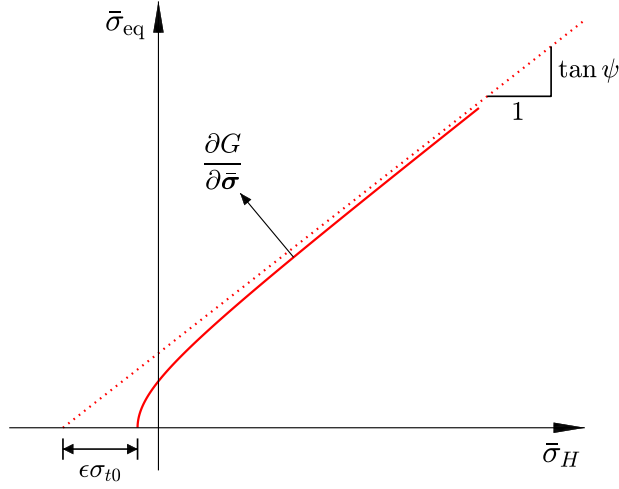


Fig. 5: The flow potential G in the $\bar{\sigma}_H$ - $\bar{\sigma}_{\text{eq}}$ plane.

is the eccentricity which defines the rate at which the function approaches the asymptote given by ψ . This gives a non-associated flow rule,

$$\dot{\epsilon}_{\text{pl}} = \dot{\lambda} \cdot \frac{\partial G(\bar{\sigma})}{\partial \bar{\sigma}} \quad (14)$$

with $\dot{\lambda}$ as the plastic multiplier. Both ϵ and ψ are required inputs to the material model, and are given in Table 1.

185 A quasi-static simulation of the cube compression test using ABAQUS/Explicit [32] was set up for calibration. The 50 mm cubes were meshed by $5 \times 5 \times 5$ elements of type C3D8R, which means 8-node reduced integration linear elements with enhanced hourglass control. Analytic rigid surfaces were used to compress the concrete, and the contact force was logged. The contact algorithm used was the “general contact all with self” [32], and a coefficient of friction $\mu = 0.47$ was used [47].
 190 Different values of μ were tried, but anything above $\mu = 0.30$ gave the same results, so $\mu = 0.47$ seems like a safe choice. A time scaling factor of approximately 10^{-2} was used, and no strain rate sensitivity was included in these simulations. The strains were obtained by measuring the relative compression of the cube like in the experiments. The calibration procedure used the data from Jankowiak and Łodygowski [48] as a starting point, and reverse engineering was used to fit
 195 the model constants to the experimental data. The results are plotted in Fig. 2(b) and the model constants are listed in Table 1, including the Poisson ratio ν_c . A tensile splitting test was simulated as well using the same setup and element size, but for this test only one experimental data point

Table 1: Material data for the CPD model.

ρ_c [kg/m ³]	E_c [GPa]	ν_c [-]		
2 445	25	0.2		
ψ [deg]	ϵ [-]	σ_{b0}/σ_{c0} [-]	K_c [-]	
38	1.0	1.12	0.666	
Compression hardening		Compression damage		
Yield stress [MPa]	Inelastic strain $\tilde{\epsilon}_{in,c}$ [-]	Damage d_c [-]	Inelastic strain $\tilde{\epsilon}_{in,c}$ [-]	
13.50	0.00000000	0.000000	0.00000000	
18.18	0.00006730	0.000000	0.00006730	
27.06	0.00008900	0.000000	0.00008900	
36.27	0.00011871	0.000000	0.00011871	
53.46	0.00052504	0.000000	0.00052504	
47.00	0.00300180	0.111585	0.00300180	
33.00	0.00710789	0.199851	0.00710789	
13.31	0.00825700	0.538831	0.00825700	
5.05	0.01438800	0.894865	0.01438800	
Tension stiffening		Tension damage		
Yield stress [MPa]	Cracking strain $\tilde{\epsilon}_{ck,t}$ [-]	Damage d_t [-]	Cracking strain $\tilde{\epsilon}_{ck,t}$ [-]	
2.81	0.00000000	0.000000	0.00000000	
3.50	0.00006670	0.000000	0.00006660	
2.63	0.00032085	0.406411	0.00033209	
1.21	0.00055953	0.696380	0.00055953	
0.32	0.00136991	0.920389	0.00136991	
0.08	0.00217346	0.980093	0.00217346	

was available. The experimentally obtained tensile strength was 3.5 MPa, while the corresponding numerical result was 3.2 MPa (within one standard deviation of the experimental results). Based on these results, the calibrated material model seemed to provide a good representation of the concrete.

The problems to be modelled in the following are of a fast transient character, which means that load/strain rate dependency could be an issue. Unfortunately, there is no data on the strain rate sensitivity of this concrete. For this reason, the CEB-FIP model code [49] was used to estimate

205 the strain rate dependency. Different dependencies were used for compression and tension, i.e.,
 Eqs. (2.1-45a) and (2.1-49a) from the code [49]. Parts (b) of these two equations were not used
 because of the limit to the increase in stress due to strain rate given by Eqs. (6a) and (6b) as
 mentioned above. This means that the strain rate effects may be underpredicted, particularly for
 high rates. Tabular data was entered for every other order of strain rate magnitude from 10^{-5} 1/s
 210 to 10^5 1/s. For best results, it is highly recommended to use the latest release of ABAQUS [32] (in
 this case 2019).

3. Reinforcing steel

3.1. Quasi-static tensile tests

A standard off-the-shelf steel grid consisting of smooth circular bars with diameter $d_r = 2.6$ mm,
 215 point-welded together to form 73.5 mm squares, was used as reinforcement in two of the four slabs
 tested herein. Standard tensile tests were carried out on 12 specimens (6 from each direction)
 in the reinforcement grid. The specimens were clamped in a 100 kN Instron universal test rig,
 and stretched at an initial strain rate of $3.6 \cdot 10^{-4} \text{ s}^{-1}$. An extensometer measured the elongation
 accurately up to necking (setup shown in Fig. 6(a)), which occurred at an engineering strain of
 220 3.4 %, while a load cell registered the force. From this data, the engineering stress-strain curves
 were established, and plotted in Fig. 6(b). The yield stress was determined to $\sigma_{02} = 766.4 \text{ MPa}$

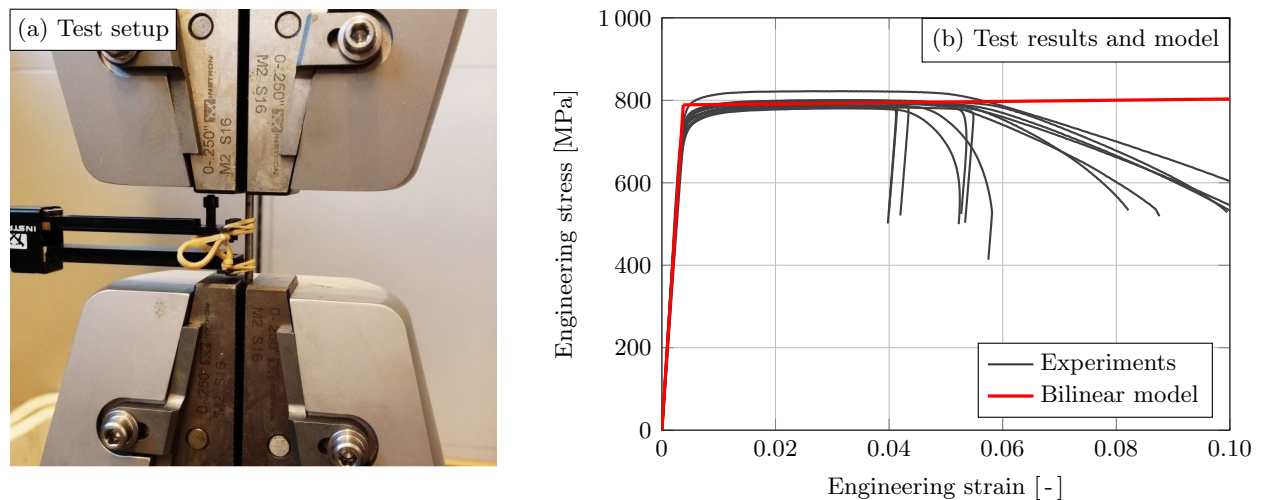


Fig. 6: Tension tests of steel reinforcement, where (a) shows the setup and (b) the results.

(at 0.2 % plastic strain), and Young's modulus was measured to $E_s = 210\,277$ MPa. The Poisson ratio and mass density were assumed to be $\nu_s = 0.3$ and $\rho_s = 7\,800$ kg/m³, respectively.

3.2. Material model

225 J2 flow theory is used to model the reinforcing steel. This means that the von Mises yield criterion is employed with the associated flow rule. Only linear isotropic hardening R_H is considered based on the results shown in Fig. 6(b). The von Mises equivalent stress σ_{eq} is given as a function of the deviatoric part $\boldsymbol{\sigma}^{\text{dev}}$ of the Cauchy stress tensor $\boldsymbol{\sigma}$,

$$\sigma_{\text{eq}}(\boldsymbol{\sigma}) = \sqrt{\frac{3}{2} \boldsymbol{\sigma}^{\text{dev}} : \boldsymbol{\sigma}^{\text{dev}}} \quad (15)$$

The strain hardening R_H is expressed as

$$R_H(\varepsilon_{\text{eq}}) = H_p \varepsilon_{\text{eq}} \quad (16)$$

230 where ε_{eq} is the equivalent plastic strain, and H_p the plastic hardening modulus. The initial size of the yield surface is given by the yield stress σ_y . Strain rate sensitivity is included multiplicatively by the Johnson-Cook (JC) strain rate term [50]. Then, from Eq. (15) and Eq. (16), the dynamic yield function f becomes

$$f(\boldsymbol{\sigma}, \varepsilon_{\text{eq}}, \dot{\varepsilon}_{\text{eq}}) = \sigma_{\text{eq}} - (\sigma_y + H_p \varepsilon_{\text{eq}}) \left(1 + C \cdot \ln \left(\frac{\dot{\varepsilon}_{\text{eq}}}{\dot{\varepsilon}_0} \right) \right) \quad (17)$$

235 The material constants σ_y and H_p were determined by a least squares fitting, and are given in Table 2 along with the rest of the material data. C is the JC strain rate dependency constant, and was chosen equal to 0.01 based on previous work with high rate loading of steel [51, 52]. The reference strain rate $\dot{\varepsilon}_0$ is the strain rate at which the tests were performed. The quasi-static response of the model ($C = 0$) is plotted in Fig. 6(b) along with the experimental data.

Table 2: Material constants for steel reinforcement.

ρ_s [kg/m ³]	E_s [GPa]	ν_s [-]	σ_y [MPa]	H_p [MPa]	C [-]	$\dot{\varepsilon}_0$ [1/s]
7 800	210	0.3	789	1039	0.01	0.00036

4. Component tests

240 The shock tube tests used for validation were also presented in [34], but are recapitulated concisely here for the sake of completeness. First, the shock tube is described in brief, and then an overview of the experiments is presented.

4.1. Shock tube description

The shock tube is sketched in Fig. 7. Membranes in the firing section separate the driver from the driven section, allowing a compressor to build up air pressure in the former. Intermediate chambers in the firing section ensures a stepwise increase of the pressure from the atmospheric pressure P_0 in the driven section, to the desired firing pressure P_d in the driver. When the pressure level P_d is attained, the intermediate chambers in the firing section are vented rapidly so that the membranes are punctured, and eventually a shock wave propagates down the driven section towards the target mounted at the end of the shock tube. Pressure sensors flush mounted with the internal wall monitor the travelling shock wave. Sensors 1 and 2 in Fig. 7 provide an estimate of the reflected pressure at the slabs, and are located 345 mm and 245 mm (respectively) upstream from the test specimen. Further description of the shock tube can be found in the work by Aune et al. [33].

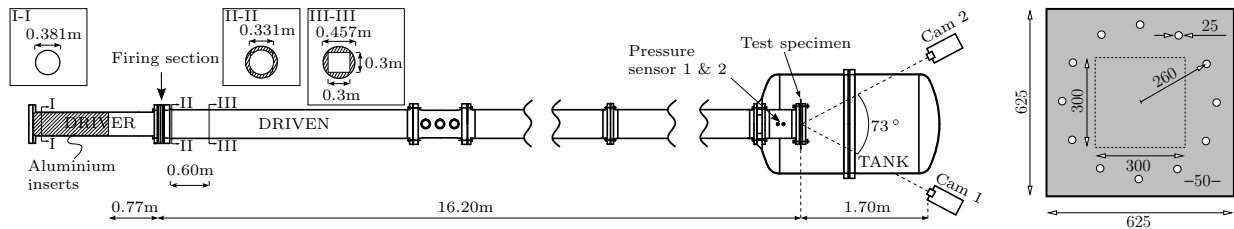


Fig. 7: Sketch of shock tube [33] where aluminium inserts can be used to adjust the volume of the driver (left) and hence the magnitude and duration of the shock wave arriving at the test specimen (inside tank) where pressure sensors and two high-speed cameras capture the experiments. The concrete slab geometry is sketched on the right.

255 4.2. Setup of experiments

Four clamped concrete slabs were subjected to blast loads of two different magnitudes in this study; two slabs with reinforcement and two without. The slabs are 50 mm thick, and their geometry can be seen on the right in Fig. 7. Two layers of the reinforcement grid were positioned

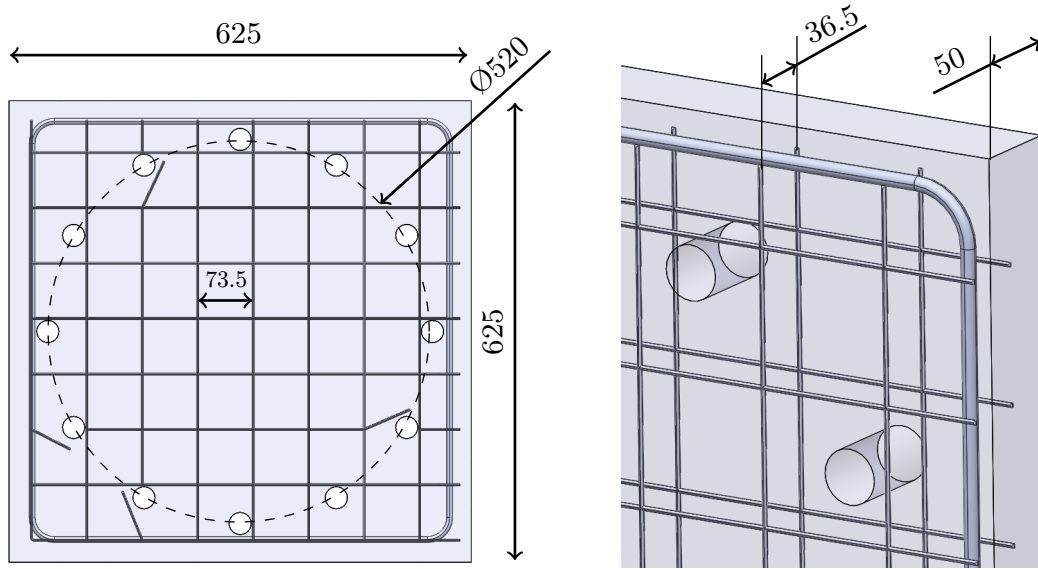


Fig. 8: Sketch of reinforcement position in reinforced concrete slabs (measurements in mm).

as shown in Fig. 8. The grid had to be cut in some areas to accommodate the bolt holes, but this
 260 does not affect the results to any significant extent because it is outside the 300 mm \times 300 mm load
 area. The distance between the centres of the bars was 73.5 mm in both directions. In addition,
 an 8 mm rebar looped around the bolt holes (outside the load area) to keep the slabs together
 after testing, and to provide a lifting point (see top of Fig. 9) . An aluminium clamping frame was
 placed on the outside of the concrete slab, while bolts and nuts with washer plates made sure that
 265 the slab was properly fastened. The pretension force F_b in the bolts was estimated to 20 kN [24].
 High-speed cameras provide data to measure the out-of-plane deformations by 3D-DIC [37], which
 is the reason for the speckled paint pattern sprayed on the concrete slabs (see Fig. 9).

Before the concrete slabs were tested, some calibration experiments were carried out on a
 massive steel plate mounted with 10 pressure sensors. Two different driver pressures P_d were used,
 270 and the pressure registered at the massive plate was used for the numerical simulations. The
 concrete slabs are identified by the material (P for plain slabs and R for reinforced slabs) and by
 the peak overpressure P_{peak} as logged by sensor 2, which means that a plain concrete slab exposed
 to about 1.1 MPa load is named P-11 and so on.

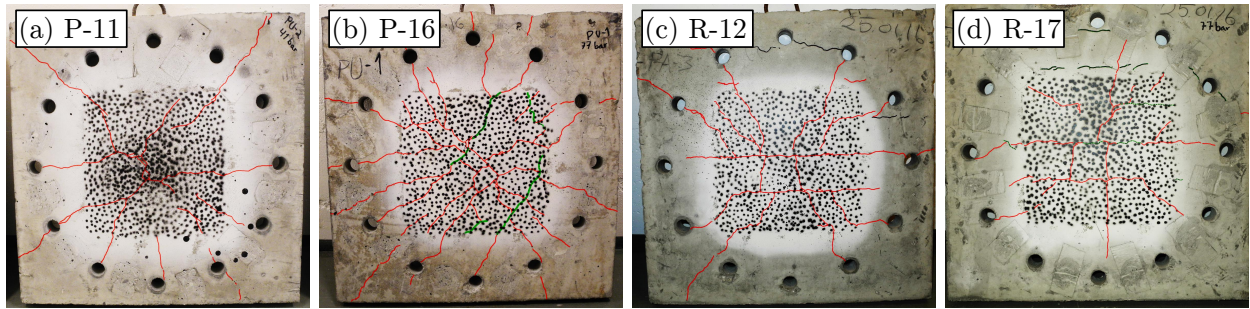


Fig. 9: The four concrete slabs tested in the shock tube (the shock wave arrives opposite to the visible side), and cracks arising from the shock tube tests are highlighted with red lines.

4.3. Experimental results

275 The shock tube produces a consistent and predictable dynamic load, as seen in Fig. 10 and in Ref. [33]. For the lower of the two loads, the curves fit almost perfectly for the concrete slab and the massive steel sensor plate, and resemble an idealised blast load curve. When P_d is increased, some secondary reflections are introduced and a discrepancy arise. This is partly because pressure sensor 2 does not measure the pressure exactly at the concrete slab, but 245 mm upstream from
 280 it, and larger pressures cause larger differences. When running numerical simulations, the pressure histories from the calibration tests will be used.

Surface cracks were observed in all four slabs, and judging from the high-speed footage the cracks did not seem to extend through the entire thickness although some bursts of dust were noted. The cracks typically initiated in the centre of the slab, and extended “radially” towards the
 285 edges for the plain concrete slabs. In the reinforced slabs, the cracks aligned with the reinforcing

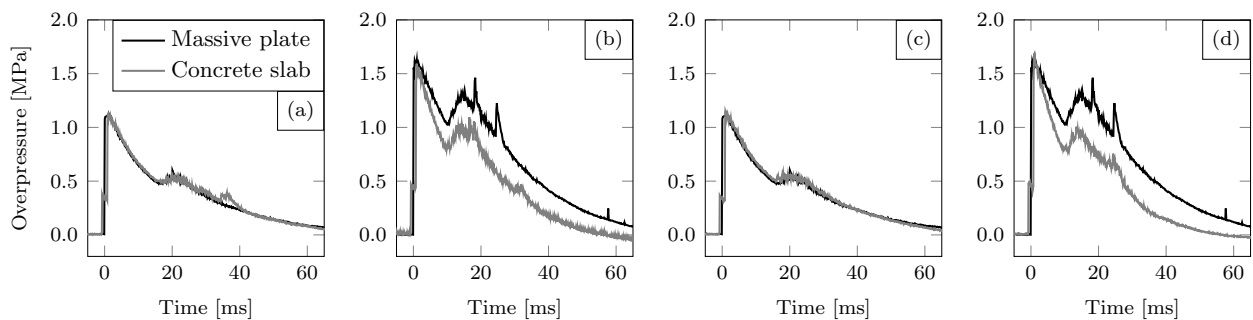


Fig. 10: Pressure-time histories (grey) from sensor 2 in shock tube tests of concrete slabs: (a) P-11, (b) P-16, (c) R-12 and (d) R-17. The results from tests performed on a massive steel plate with pressure sensors are shown as solid black lines.

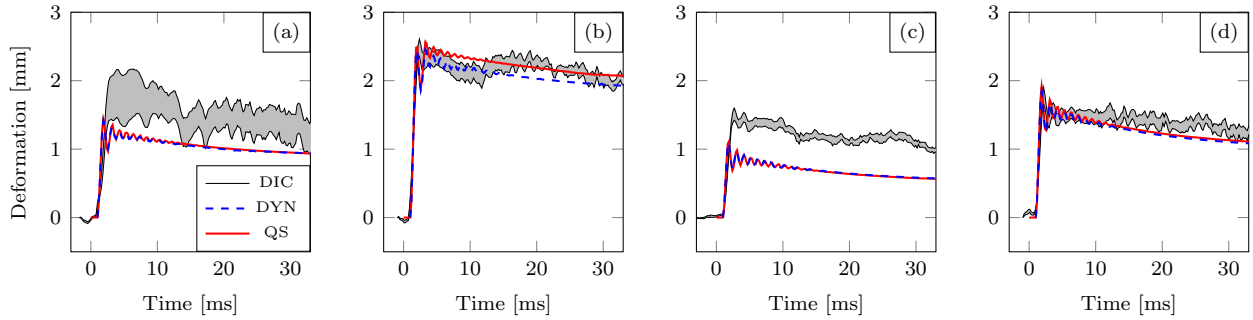


Fig. 11: The hatched grey areas show the midpoint out-of-plane deformation as measured by 3D-DIC compared with finite element simulations with (DYN) and without (QS) strain rate dependency for (a) P-11, (b) P-16, (c) R-12, and (d) R-17.

steel grid. In Fig. 9, the cracks are accentuated with red lines, clearly illustrating the effect of the reinforcement. The effect of the steel grid is also evident in the 3D-DIC measurements, as it gave smaller out-of-plane deformation for reinforced plates compared with their unreinforced counterparts. Fig. 11 shows the estimated out-of-plane deformations, where the hatched grey area is the range of deformations among the four DIC-nodes closest to the centre of the slab. The red and blue lines show the out-of-plane deformation obtained by FEM using ABAQUS/Explicit [32], discussed in more detail later.

The effect of the increased load on the out-of-plane deformation were also in accordance with expectations. Three different camera calibrations for the 3D-DIC approach were used without much discrepancy (only tenths of millimetres difference), which means that the results should be accurate even when the deformations are small like in this case. Due to the deformations being this small, fluid-structure interaction appears to be minor for this case. If, however, through-thickness cracks become sufficiently large, the load and structural behaviour may change.

5. Numerical simulations of component tests

5.1. Setup of simulations

All simulations are Lagrangian and conducted using the commercially available finite element code ABAQUS/Explicit [32]. Because this is a fast transient dynamic problem involving contact, the simulations are explicit. The magnitude of the blast load is taken from the massive steel plate calibration tests (black curves in Fig. 10) and applied as a uniform pressure across the load area measuring 300 mm × 300 mm (sketched on the right in Fig. 7). Fig. 12 shows the numerical setup

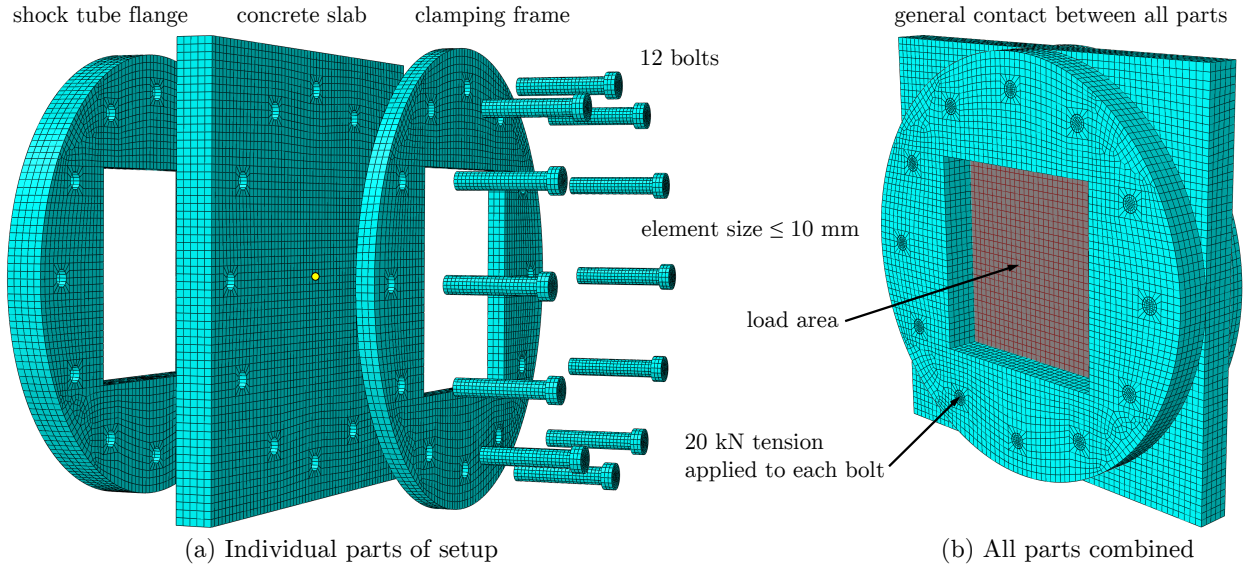


Fig. 12: Image of the setup used for the FE simulations, with (a) showing all the different parts included in the analyses, and (b) the parts combined and the area where the pressure load is applied (coloured red). The out-of-plane deformation is measured at the small yellow dot in (a).

and the final mesh used in the simulations, where the element size was chosen to approximately 10 mm. This element size is the same as in the cube compression test used in the calibration of the CDP model in Fig. 2(b).

The elements used are C3D8R as for the compression test, and a “general contact” with $\mu = 0.47$ is used also in these simulations. The multipart setup may seem a bit convoluted, but including the different parts has been found to be necessary to obtain the desired level of accuracy [53]. The concrete slab is placed in contact with the shock tube flange, and the clamping plate is placed on the outside of the slab like in the experiments. Forces are then applied to the ends of the bolts, thereby securing the clamping frame and the concrete slab with the same pretension force $F_b = 20$ kN as in the tests. The bolt force was ramped up smoothly to 20 kN with a duration of 10 ms. At the end of the bolt tightening step, the kinetic energy was 0.07 J, which was about 2 % of the internal energy.

When relevant, steel reinforcement bars are included as a fifth part by using two-node linear beam elements (called B31). The steel grid geometry is shown in Fig. 8. The beam elements are then superposed with the solid mesh and connected using an embedding constraint in the interaction module of ABAQUS [32], thereby assuming perfect bonding between the concrete and

the reinforcement.

The material model for concrete is described in Section 2.2, and the model for the steel reinforcement can be found in Section 3.2. Models with and without strain rate sensitivity were run for comparison, but no temperature effects were included. Both the shock tube flange and the clamping frame were modelled as linear elastic materials; the former as steel and the latter as aluminium. The Young's modulus used for all steel parts (including the bolts) was $E_s = 210\,000$ MPa, while $E_a = 70\,000$ MPa was used for aluminium. The mass densities applied were $\rho_s = 7\,800$ kg/m³ and $\rho_a = 2\,700$ kg/m³ for steel and aluminium, respectively. A Poisson ratio of $\nu_s = 0.3$ was used for all metal parts.

5.2. Results of component test simulations

The peak pressure has been shown to be important in this type of simulation [54], and this is confirmed here. Fig. 11 shows that increasing the load increases the mid-point deflection, and that adding reinforcement reduces this deflection as expected. The relative deformation between the four simulations is in accordance with the experiments, while the exact quantitative value is somewhat off for the lower pressure. For slabs P-16 and R-17 the deflection is quite accurate, and the stiffness of the setup – represented by the initial tangent of the curves in Fig. 11 – is captured accurately. The results are, however, slightly non-conservative for the lower pressure and should be used with care. It is difficult to pinpoint a single reason for this because many parameters influence the results. However, the bolt clamping force (i.e., boundary conditions) and the tensile strength of the concrete seem to be the most dominant parameters for this type of problem [34]. Also, a modification of the material constants in Table 1 could have improved the

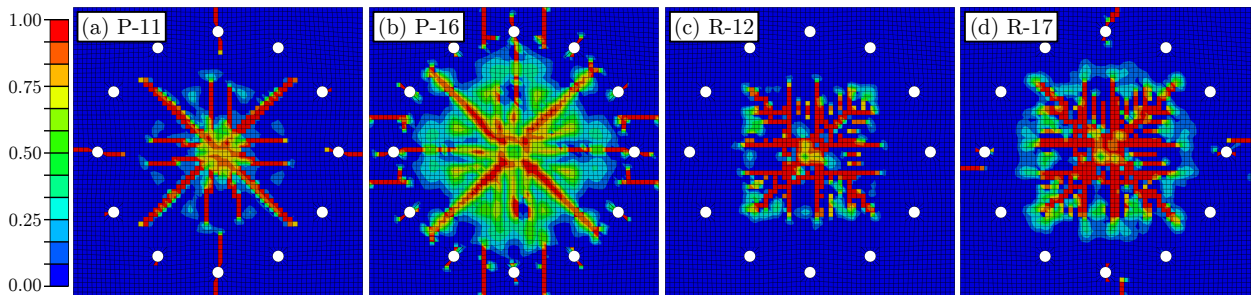


Fig. 13: Finite element results showing tensile damage d_t on the side of the slab facing the cameras, illustrating the effect of the reinforcement (compare with Fig. 9). Strain rate sensitivity is not included in these simulations.

results. Instrumenting the tensile splitting test properly and using that for inversen modelling might improve the calibration and thus the results for the lower pressure. Still, the values obtained by reverse engineering the cube compression test gave decent results. Including strain rate sensitivity in the model does not change the out-of-plane deformation to any significant extent. For the plain concrete slab subjected to the higher load a small difference is noted, where the strain rate sensitive model attains a lower deflection.

Fig. 13 shows the tensile damage d_t in the four slabs, where 0 is no damage and 1 indicates that there is no residual capacity. In the plain concrete slabs the cracks are typically diagonal, while the reinforcement bars tend to direct the cracks in a similar way as in the tests. Naturally, the higher load produced more damage. The damage pattern is very symmetric due to the homogeneity of the model, whereas concrete in reality is inherently heterogeneous on this scale and the crack patterns are therefore more erratic. To account for this, some kind of stochastic approach [55], discrete element model [56], or mesoscale model [57] is warranted. The patterns still resemble those from the physical experiments (compare Fig. 9 with Fig. 13), and it appears that the main physics of the problem is represented. Thus, the models should be able to make some qualitative predictions about the full-scale SFT. A simulation like this, including the contact and the tightening of the bolts, takes approximately 2 hours on a single CPU of a high-performance computer of today. Including reinforcement increases the CPU time with about 25 %, while including the strain rate sensitivity approximately doubles the CPU time.

6. Case study – Full-scale simulations of blast loaded submerged floating tunnels

6.1. Geometry and load description

Several different cross-sections for an SFT have been proposed, with the two main categories being circular and rectangular versions (see Fig. 14). These shapes were proposed for some fjord crossings, which means that they represent possible solutions [3, 11, 39]. Elliptical cross-sections are also possible [6], but are not considered here. The designs have two parallel tubes to increase the transverse stiffness [58] and to allow operation of one tube while the other is under maintenance. Based on the validated model used for the shock tube simulations, this 3D numerical case study will – by using Lagrangian techniques available in ABAQUS/Explicit [32] – examine the relative response of the two geometries when a detonation occurs inside the structure. The main idea is

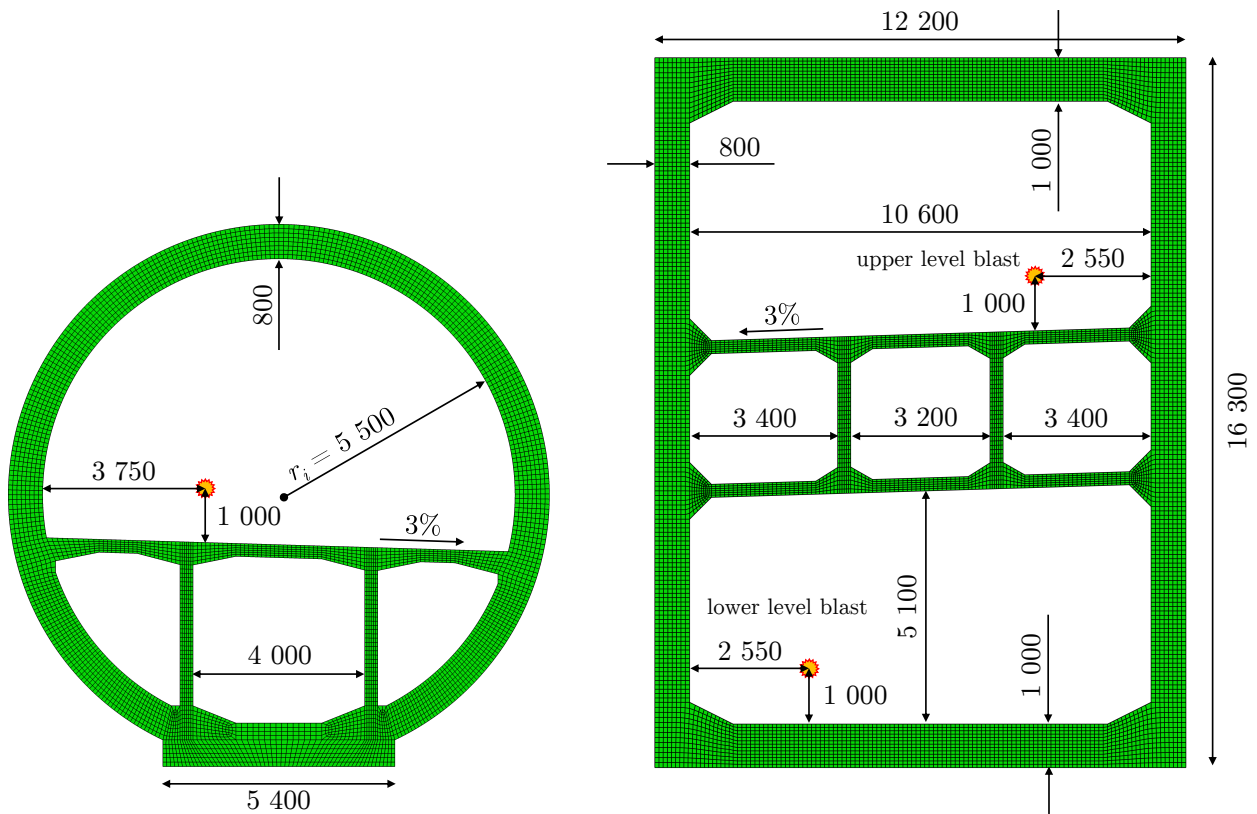


Fig. 14: Geometry and mesh for circular (consisting of a total of 2.8M elements) and rectangular (5.9M elements) SFT profiles (all measurements in mm unless otherwise specified). Both geometries were extruded to 5 times the largest outer cross-sectional diameter (63.0 m and 81.5 m).

that the case study uses the validated material model to make some qualitative predictions about the damage pattern, and attempts to identify potential weak zones. For the final design, the material properties and geometries will most likely be somewhat different from what is used here.

375 The effect of strain rate sensitivity and charge size will also be investigated. Different lengths of the SFT were also tested, and the length was increased until the boundary effects became small. The final choice was 5 times the maximum outer cross-sectional measurement.

The CONWEP approach is adopted to simulate the air blast load, and it assumes a spherical charge detonated in free air. This CPU efficient technique is based on the experimental data
 380 obtained by Kingery and Bulmash [40], and the method is readily available in ABAQUS [32]. A location for the detonation is specified, and then the equivalent mass of TNT is added to complete the input. The point of detonation is chosen to be in the centre of the driving lane closest to the wall, because this is where the vehicles typically will travel. The exact location of the detonation

Table 3: Blast load parameters from CONWEP in ABAQUS [32] for a standoff distance of 1.0 m.

TNT [kg]	Z [m/kg ^{1/3}]	P_r [MPa]	t_A [ms]	i_r^+ [MPa·ms]	t^+ [ms]
500	0.126	281.7	0.17	218.5	1.56
100	0.215	132.0	0.20	24.2	0.87
10	0.464	34.4	0.29	3.6	0.63

is indicated by a yellow star in Fig. 14, and the entire surface of the compartment containing the charge receives a blast load based on the distance from the detonation and the orientation of each surface normal relative to the blast origin. Note that the possible additional effects of fragment impact are not considered herein. The presence of vehicles is also neglected because this is beyond the scope of the current study.

Three different charge sizes are used, namely 10 kg, 100 kg and 500 kg of TNT. Any possible quasi-static pressure build-up is neglected. The Hopkinson-Crantz scaled distance Z is defined in terms of the standoff distance R and the charge weight W ,

$$Z = \frac{R}{\sqrt[3]{W}} \quad (18)$$

For $R = 1.0$ m, Eq. (18) gives scaled distances Z of 0.464 m/kg^{1/3}, 0.215 m/kg^{1/3}, and 0.126 m/kg^{1/3} for 10 kg, 100 kg and 500 kg, respectively. The pressure-time history $P(t)$ of the reflected pressure is described by the modified Friedlander equation [59]

$$P(t) = P_0 + P_r \left(1 - \frac{t - t_A}{t^+} \right) \cdot \exp \left(-b \cdot \frac{t - t_A}{t^+} \right) \quad (19)$$

where t_A is the shock wave time of arrival, P_r is the peak reflected overpressure generated by the blast wave, t^+ is the positive phase duration, and b is the decay coefficient. The blast load parameters as obtained by CONWEP, including the reflected impulse i_r^+ and duration t^+ of the positive phase, are given in in Table 3. The negative phase is not included because its effects are considered minor for this case.

Using CONWEP at low scaled distances may underpredict peak reflected pressures, particularly for $Z < 0.100$ m/kg^{1/3}, while estimates made for the reflected impulse and the arrival time are much more accurate [60]. The load curves for 500 kg TNT at a standoff distance of 1.0 m are therefore at the limit of the applicability range for the CONWEP data. This is therefore considered a close-in

blast. Still, experiments suggest that CONWEP may be valid as a first-order approach even for
405 small scaled distances [61]. Further, the ABAQUS manual states that the lower range limit is equal
to the estimated radius of the charge (based on the provided charge mass) [32]. For values of Z
lower than $0.145 \text{ m/kg}^{1/3}$ in ABAQUS, a linear decay is used although no warning message is given.
This occurs only in a very small area directly beneath the charge. Nevertheless, it is something to
be aware of when running these kinds of simulations, and the results should be interpreted with
410 care.

Using CONWEP for low values of Z is admittedly somewhat questionable. In this study, we
are not trying to predict the exact response of the structure, but rather the relative performance
between the geometries and between the charge sizes, and try to identify vulnerable areas for this
type of loading. For this reason, the possible underprediction of the load for 500 kg TNT is not
415 essential because we are not claiming that we are able to compute the quantitative response of this
structure in the case of 500 kg TNT explosion. We are, however, claiming that our model gives a
reasonable first-order approximation of the structural behaviour if a detonation of some kind were
to take place inside the structure at the specified locations.

While this technique provides good estimates and is easy to use, it does not account for re-
420 flections and confinement of the blast wave although decent results have been obtained for steel
pressure vessels [62] and for small concrete pipes [30]. In a confined space like inside the SFT,
reflections could influence the results [63], but the initial blast impulse from the charge will still be
the dominating load contribution. For a close-in detonation like in this case, afterburning may also
affect the load to the structure [64, 65], an effect which is not included in the CONWEP module.
425 It is possible to modify the applied load for the smallest values of Z [60] or use methods devel-
oped for internal explosions [65], but this is beyond the scope of the current study as we want to
use methods already available in ABAQUS. To capture reflections, a fully coupled fluid-structure
interaction simulation becomes necessary [66]. Another option is to first run a purely Eulerian
fluid simulation, and then apply the results (in terms of pressure) to the structure in a subsequent
430 Lagrangian simulation [67]. These types of simulations may be highly mesh dependent and very
time consuming while not necessarily providing better results [68]. Besides, part of the aim in this
study is to examine what is possible to achieve with fairly simple numerical techniques which are
useful for assessing the general behaviour of blast loaded structures.

6.2. Mesh and reinforcement

435 The tunnel geometries are – like the cubes and slabs – discretised by C3D8R elements. A mesh sensitivity study was conducted on a simply supported one-way strain rate sensitive concrete plate with unit width, thickness 300 mm, and a span of 4000 mm (see Fig. 15(a)). The setup uses a geometry similar to the internal structures of the SFTs in Fig. 14. The plate is loaded with the same charge sizes as for the full STFs, and the midpoint deflection of the bottom of the plate is evaluated. The 10 kg charge gives only small deformations, while the 100 kg charge seems likely to damage the structure. The 500 kg charge causes a massive deflection, and the plate is for sure destroyed.

440

The smallest element size is the one used in the material calibration (10 mm), and it is increased successively to 300 mm. Fig. 15(b)-(d) show the results, which indicate a certain difference for increase in element size. An element size of 300 mm is too coarse, because it results in only one

445

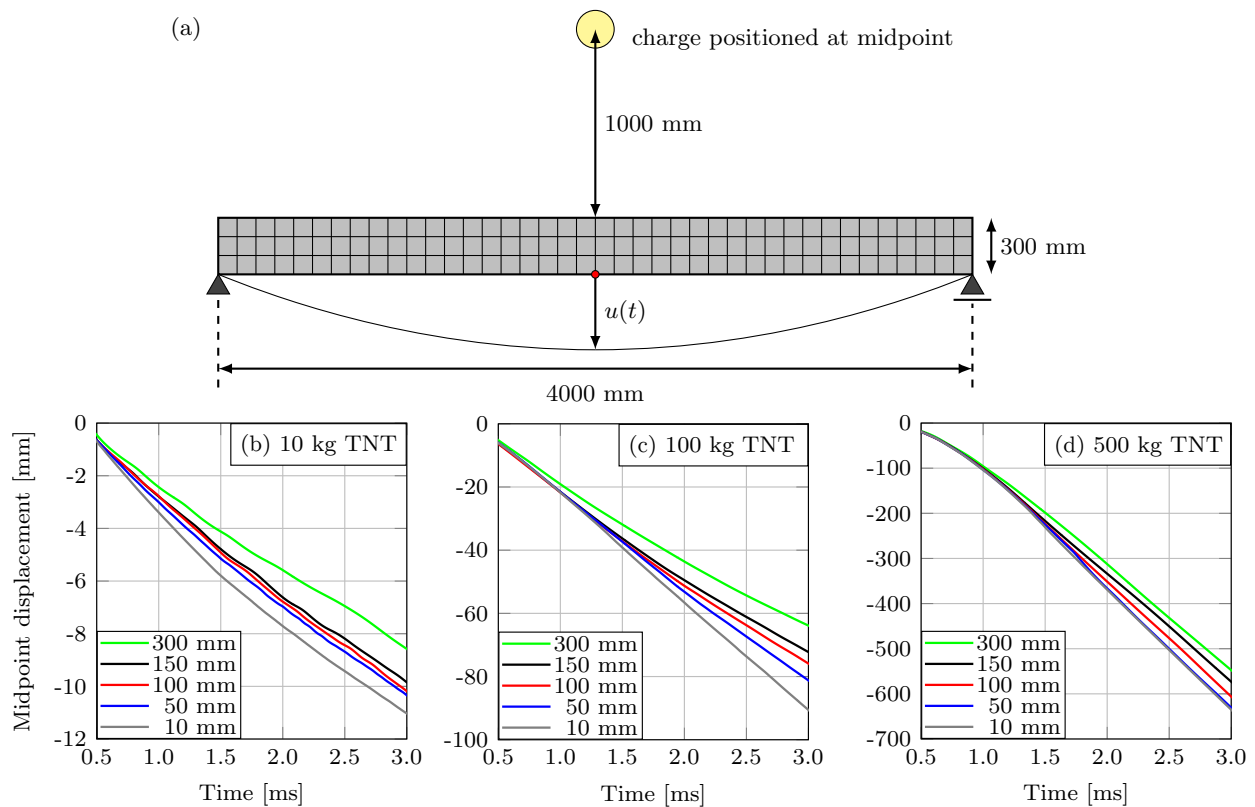


Fig. 15: Mesh sensitivity study where the setup is shown in (a), and the results in terms of midpoint displacement $u(t)$ are plotted for TNT equivalents of (b) 10 kg, (c) 100 kg, and (d) 500 kg.

element across the thickness, and the mesh is thus not able to properly describe bending. Based on these results 100 mm appears to be a good compromise, but the internal walls of the SFTs are still discretised by at least 6 elements across the thickness (see Fig. 14) while the outer walls are given an element size of maximum 100 mm. Halving the element size for these parts would increase the amount of elements by a factor of 8 in an already large model. The relative differences between the load cases and between the element sizes are consistent. Based on these results the chosen discretisation should be able to contribute in making qualitative considerations for the blast loaded SFTs. We are mainly concerned with the overall response of the structure and the relative differences between charge sizes and geometries. If local effects are to be investigated, the mesh should be refined in the areas of interest.

The reinforcement included was chosen to exceed at least the minimum amount $A_{s,\min}$ required by Eurocode 2 [41],

$$A_{s,\min} = 0.0013 \cdot b_t d_h \quad (20)$$

in which b_t is the mean width of the tension zone, and d_h is the effective height in the cross-section. Thus, two layers of 20 mm diameter reinforcement bars were placed with 50 mm concrete cover from the inner and outer surfaces. They were placed 300 mm apart in both the longitudinal and circumferential directions for the entire SFT. Like the solid elements, the beam elements were maximum 100 mm long. A total time of 50 ms was simulated, leaving sufficient time for the blast wave to propagate down a sufficient length of the SFT. The same material models for the concrete and reinforcement as used for the concrete slab simulations were also employed here. The same embedding technique as used for the reinforced slabs was used here as well. No particular boundary conditions were used for the SFTs because they are designed to be of approximately neutral buoyancy [3].

6.3. Full-scale simulation results and discussion

The full-scale SFT simulation of the rectangular profile with 100 kg TNT (lower compartment) took almost 1.5 hours on 14 CPUs of a high-performance computer of today. Including strain rate sensitivity more than doubled the CPU time. A fully-coupled simulation would increase the duration and required memory by several orders of magnitude, particularly since the fluid mesh should be at least as fine as the structural mesh [69].

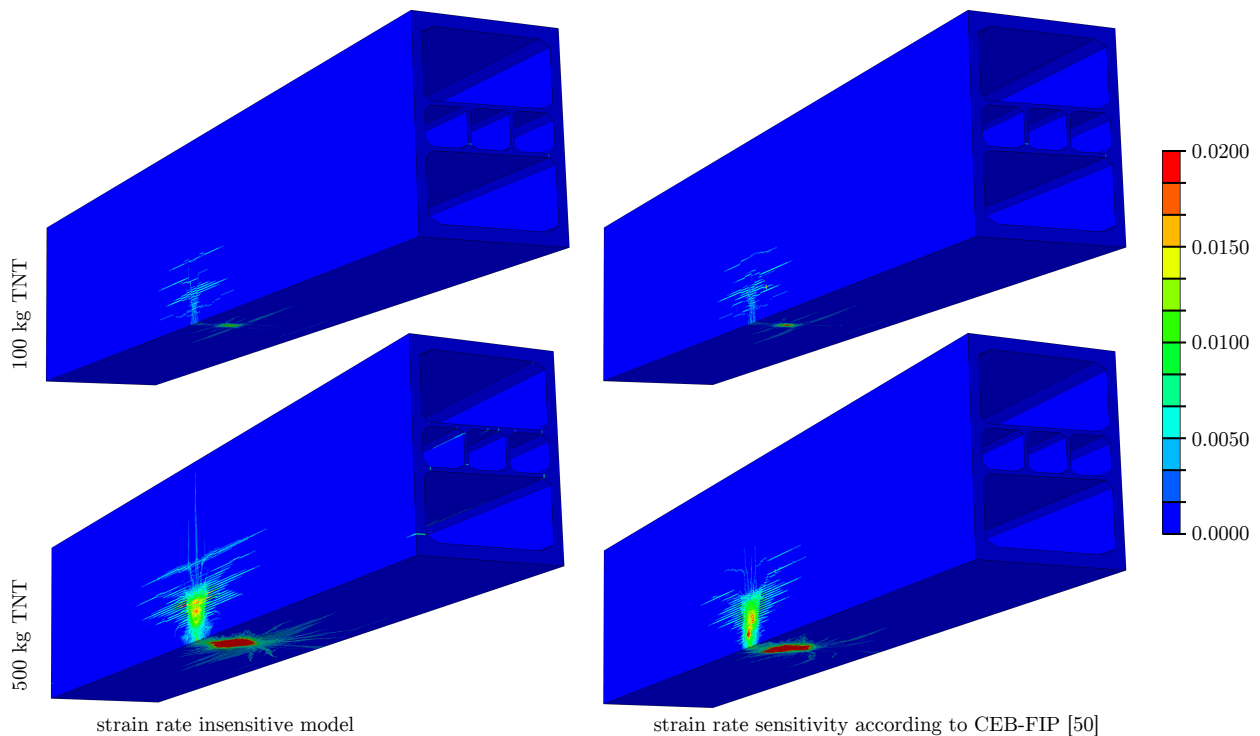


Fig. 16: Contour plots of $\tilde{\epsilon}_{pl,t}$ 50 ms after detonation in the lower level of a rectangular SFT. Directly underneath the detonation point the probability is high for breaching because the detonation is close to the outer wall. Locally, values of $\tilde{\epsilon}_{pl,t}$ may exceed the levels indicated by the legend.

The effect of the different charge sizes was evident through the extent of the deformation and equivalent plastic strains in the structure. For all detonation positions studied, a charge size of 10 kg was found to damage the internal walls only to a minor extent. This was also the case for the mesh study in Fig. 15. The outer walls barely deform, so this result means that the 10 kg charge size is not discussed in any further detail.

Fig. 16 shows the rectangular SFT subjected to detonations in the lower compartment. No nodal averaging has been used in any of the contour plots. It is observed that including strain rate sensitivity reduces the extents of the strains as expected. The results are still qualitatively quite similar, and the remainder of the results will be shown for the strain rate insensitive model because of the shorter simulation times. Also, including strain rate effects in the model caused some instabilities for certain cases. Another important result is that the bottom of the structure suffers a lot of damage for the 500 kg charge. This is caused by the charge being close to this part, so it might a good idea to have the vehicles drive on an internal structure rather than directly on

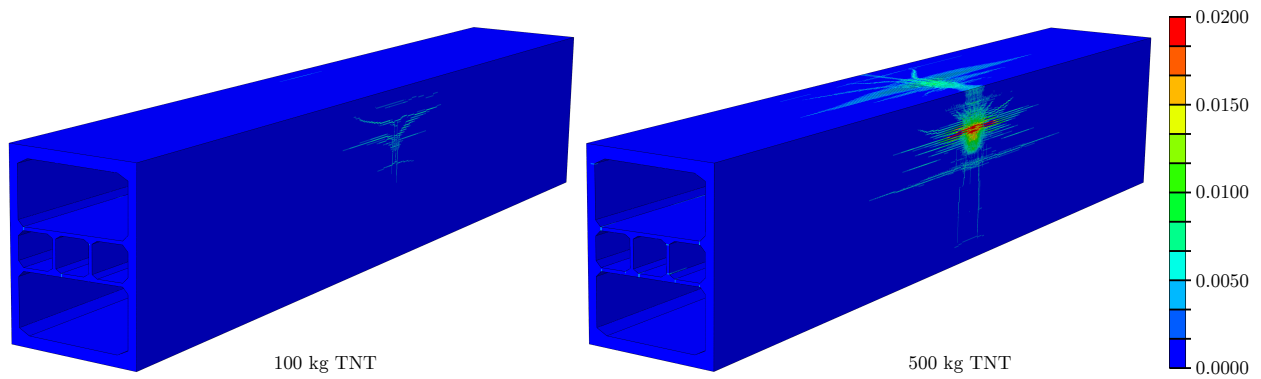


Fig. 17: Contour plots of $\tilde{\epsilon}_{p1,t}$ 50 ms after detonation in the upper level of a rectangular SFT. Locally, values of $\tilde{\epsilon}_{p1,t}$ may exceed the levels indicated by the legend.

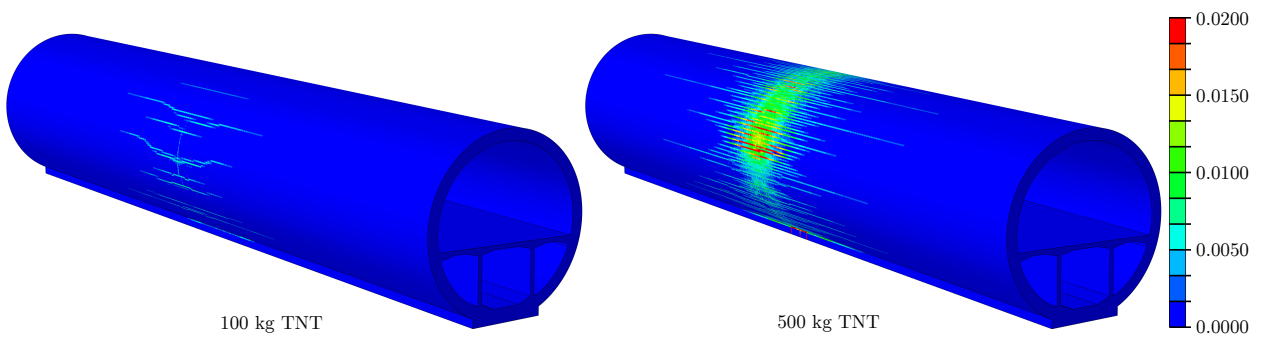


Fig. 18: Contour plots of $\tilde{\epsilon}_{p1,t}$ 50 ms after detonation in a circular SFT. Locally, values of $\tilde{\epsilon}_{p1,t}$ may exceed the levels indicated by the legend.

the outer wall. The damage for the 100 kg charge is considerably lower, and might be manageable due to the reinforcement's ability to distribute the load.

For the detonation in the upper compartment, illustrated in Fig. 17, the damage to the outer walls is considerably less although the side wall suffers. Table 4 lists the maximum values for the equivalent plastic strains (tensile and compressive) for the outer walls, in addition to the maximum deformation. The lower compartment detonation in the rectangular profile is by far the worst case of the ones considered.

The circular profile in Fig. 18 has a larger area across which the damage is distributed, thus reducing the magnitude as shown in Table 4. This is because the point of detonation is closer to the centre of area of the cross-section, and thereby further away from the outer walls. The comparably low temporal distribution of shock wave arrival times in the circular geometry contributes to the more evenly distributed strains in the circular geometry. Loading one area heavily before another

Table 4: Maximum values of equivalent plastic tensile and compressive strains, and of deformation in outer walls at the end of the full-scale SFT simulations.

Charge size	Geometry	$\tilde{\epsilon}_{pl,t}$ [-]	$\tilde{\epsilon}_{pl,c}$ [-]	u_{max} [mm]
100 kg	circular	0.0162	0.0004	7
	rect. upp.	0.0164	0.0010	13
	rect. low.	0.0918	0.0028	37
500 kg	circular	0.0571	0.0021	63
	rect. upp.	0.1243	0.0057	65
	rect. low.	0.8738	0.1861	647

causes higher local damage compared with a more evenly distributed load. The equivalent plastic
500 tensile strain is observed to follow the reinforcement bars like in Fig. 9(c) and (d), and Fig. 13(c)
and (d). This applies to the rectangular cross-section as well, mostly when the charge is placed
at the upper level. A 100 kg TNT charge is very likely to produce fragmentation of the internal
walls for all cases, thus destroying them in the area close to the detonation. The equivalent plastic
strain levels in the outer walls are below 2 % except for the lower detonation (see Table 4). Cracks
505 running longitudinally along the main SFT axis are noted, which is in line with experimental results
obtained by testing cylindrical concrete tubes with spherical, centrally placed C-4 charges [70].
The area where the internal walls connect with the outer walls is a critical zone because loads are
transferred there.

The asphalt will naturally help mitigate the blast load, and will also increase the post-blast
510 capacity [71]. The deformation quantities in Table 4 for the outer walls are highest for detonation
in the lower compartment of the rectangular SFT. Detonation in this location is found to be the
worst case because the detonation occurs so close to the external wall at the bottom. This applies
to the side wall of the rectangular profile as well, for both the upper and lower level detonations.

In any case, 500 kg TNT appears to breach the outer wall of the rectangular profile when
515 the detonation occurs at the lower level. The unrealistically high values of the strains and of
 u_{max} in Table 4 suggest this. For the other two cases, 500 kg TNT generates comparatively low
strain and deformation values. Additional reinforcement or sacrificial claddings [72] could help
maintain the structural integrity. To highlight the differences between the circular and rectangular

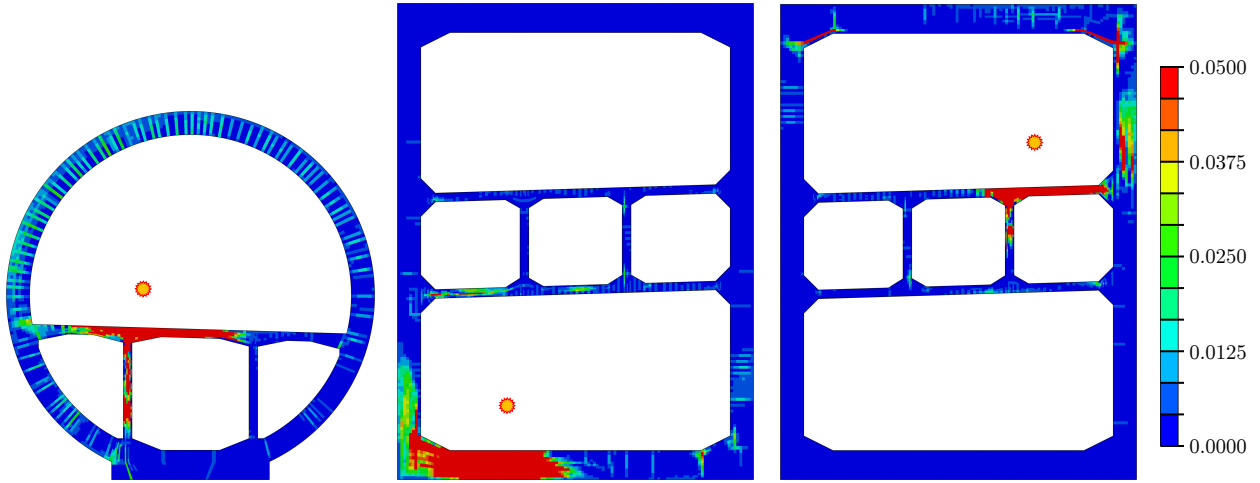


Fig. 19: Contour plot of the equivalent plastic tensile strain $\tilde{\epsilon}_{pl,t}$ at the cross-section where the 500 kg TNT detonation occurs (50 ms after detonation). Locally, values of $\tilde{\epsilon}_{pl,t}$ may exceed the levels indicated by the legend.

profiles, the equivalent plastic tensile strain at the cross-section where the detonation took place
 520 has been plotted in Fig. 19 using the charge size of 500 kg TNT equivalents. From this figure, it
 is evident that the internal walls are heavily damaged. For the outer walls, the damage is most
 intense where the internal walls connect to the outer wall because forces are transmitted through
 them. Also, an unwanted strain concentration appears close to the corners in the upper level of
 the rectangular profile (right part of Fig. 19). These areas are then more prone to breaching, and
 525 extra reinforcement may be necessary as suggested earlier. A similar tendency can be seen in the
 circular profile where the inner and outer walls connect, but to a lesser extent because the loading
 (and hence the damage) is more evenly distributed due to the circular geometry. With both this
 and the strain concentration effect of the corners in mind, a circular profile would be preferable
 to a rectangular for this type of loading. This result conforms with a preliminary study on this
 530 topic [24].

7. Concluding remarks

Using DIC on the cube compression test provided reliable data for calibration of the CDP
 model (see Fig. 2(b)). The shock tube produced consistent loads and is a valuable and predictable
 tool for understanding the behaviour of plated structures exposed to shock loading. For higher
 535 pressures, the load curves deviate somewhat from that of an idealised blast load due to secondary

reflections (shown in Fig. 10(b) and (d)). High-speed cameras synchronised with the pressure recordings enable the use of 3D-DIC to relate the load to the deformations, and are helpful in understanding the behaviour of the slabs. These cameras also make it possible to pinpoint when and where a through-thickness crack appears.

540 In the numerical simulations, the experimentally observed effects of the steel reinforcement and the effects of the load intensity were captured well. Compared with the out-of-plane deformation obtained experimentally by DIC, the results were very close for the higher load (Fig. 11(b) and (d)), but deviated non-conservatively for the lower load (Fig. 11(a) and (c)). The relative differences between each case were according to expectations, and the damaged areas aligned with
545 the reinforcement just like in the experiments (see Fig. 9 and Fig. 13). Overall, the shock tube simulations are good qualitative models which make reasonable quantitative predictions.

Finally, a case study on internal blast loading of two different SFT profiles was carried out. A charge size of 10 kg TNT is found to be within the capacity of both SFT designs for the examined charge positions. For 100 kg TNT, the internal walls were damaged but the outer walls largely
550 remained intact. The worst case was the detonation at the lower level of the rectangular SFT, where the detonation is very close to the bottom outer wall. Some unwanted strain concentrations appeared close to the corners of the rectangular profile, making this area more susceptible to leakage and breaching. Extra reinforcement should be added where the inner walls connect with the outer walls because large forces are transmitted there. Fibre reinforcement can also be a good
555 alternative [27]. Leakage is naturally a critical issue, so the structure should also be compartmented to avoid complete flooding in case of breaching. Tunnel linings can be used to mitigate the blast load [73], and should at least be applied in the zones where the floating pontoons or tethers are located [28]. Steel jackets and polyurethane are in addition alternative solutions [74].

The road lanes in the rectangular option rest directly on the bottom outer wall and are closer to
560 the outer side walls as well. In a circular geometry, the point of detonation is moved further away from at least one of the outer walls by design. Railings could also be added to hinder direct vehicle impact against the outer wall. For these reasons the circular cross-section is found to be the better choice for this type of loading. The full-scale simulations were relatively easy to set up and can provide valuable insight during the design phase. Possible confinement effects and afterburning of
565 the internal explosion were not accounted for in this study, nor was the effect of the surrounding

water, possible fragments or presence of vehicles. Extending the work to include computational fluid dynamics or fluid-structure interaction is a natural next step, and is scheduled for further work.

The overall goal of the study was to examine the general behaviour of an SFT structure exposed to internal blast loading, and this was obtained by choosing geometries used for a realistic design and applying a general set of loads. The study has established a validated numerical model based on the material and component tests. The method and results herein will therefore be useful in a future design of this type of structure.

Acknowledgements

The authors would like to express their gratitude to the Norwegian Public Roads Administration for financing this work through the E39 Coastal Highway Route project.

References

- [1] Norwegian Public Roads Administration. The E39 Coastal Highway Route. 2019. <http://www.vegvesen.no/Vegprosjekter/ferjefriE39/English>. Accessed 29.04.2019.
- [2] P. Tveit. Submerged floating tunnels (SFTs) for Norwegian fjords. *Procedia Engineering*, 4:135–143, 2010.
- [3] A. Minoretta, A. Myhr, S.A. Haugerud, J.H. Sekse, and T.E. Egeberg. The submerged floating tube bridge: The invisible bridge crossing the Bjørnafjord. *19th Congress of the International Association for Bridge and Structural Engineering, Stockholm, Sweden*, 2016. Paper no. Stock-0316-2016-R2.
- [4] B. Jakobsen. Design of Submerged Floating Tunnel operating under various conditions. *Procedia Engineering*, 4:71–79, 2010.
- [5] S. Remseth, B.J. Leira, K.M. Okstad, K.M. Mathisen, and T. Haukås. Dynamic response and fluid/structure interaction of submerged floating tunnels. *Computers and Structures*, 72:659–685, 1999.
- [6] A. Mandara, E. Russo, B. Faggiano, and F.M. Mazzolani. Analysis of fluid-structure interaction for a submerged floating tunnel. *Procedia Engineering*, 166:397–404, 2016.
- [7] B.J. Leira. First- and second-order wave-induced dynamic response of submerged floating tunnels. *Proceedings of the ASME 2016 35th International Conference on Ocean, Offshore and Arctic Engineering, Busan, South Korea*, 2016. Paper no. 54598.
- [8] H. Lin, Y. Xiang, Y. Yang, and Z. Chen. Dynamic response analysis for submerged floating tunnel due to fluid-vehicle-tunnel interaction. *Ocean Engineering*, 166:290–301, 2018.
- [9] S.-I. Seo, H.-S. Mun, J.-H. Lee, and J.-H. Kim. Simplified analysis for estimation of the behavior of a submerged floating tunnel in waves and experimental verification. *Marine Structures*, 44:142–158, 2015.

- [10] X. Xiang, M.E. Eidem, J.H. Sekse, and A. Minoretti. Hydrodynamic loads on a submerged floating tube bridge induced by a passing ship or two ships in maneuver in calm water. *Proceedings of the ASME 2016 35th International Conference on Ocean, Offshore and Arctic Engineering, Busan, South Korea*, 2016. Paper no. 54030.
- [11] T.E. Aasland, A. Myhr, S.A. Haugerud, A. Minoretti, and J.H. Sekse. A submerged floating tube bridge concept for the Bjornafjord crossing – alternatives for station keeping. *Proceedings of the ASME 2016 35th International Conference on Ocean, Offshore and Arctic Engineering, Busan, South Korea*, 2016. Paper no. 54056.
- [12] Y. Xiang and Y. Yang. Spatial dynamic response of submerged floating tunnel under impact load. *Marine Structures*, 53:20–31, 2017.
- [13] L. Martinelli, G. Barbella, and A. Feriani. A numerical procedure for simulating the multi-support seismic response of submerged floating tunnels anchored by cables. *Engineering Structures*, 33:2850–2860, 2011.
- [14] L. Martinelli, M. Domaneschi, and C. Shi. Submerged Floating Tunnels under Seismic Motion: Vibration Mitigation and Seaquake effects. *Procedia Engineering*, 166:229–246, 2016.
- [15] A. Schenker, I. Anteby, E. Gal, Y. Kivity, E. Nizri, O. Sadot, R. Michaelis, O. Levintant, and G. Ben-Dor. Full-scale field tests of concrete slabs subjected to blast loads. *International Journal of Impact Engineering*, 35:184–198, 2008.
- [16] D. Zhang, S. Yao, F. Lu, X. Chen, G. Lin, W. Wang, and Y. Lin. Experimental study on scaling of RC beams under close-in blast loading. *Engineering Failure Analysis*, 33:497–504, 2013.
- [17] J. Li and H. Hao. Numerical study of concrete spall damage to blast loads. *International Journal of Impact Engineering*, 68:41–55, 2014.
- [18] D.-K. Thai and S.-E. Kim. Numerical investigation of the damage of RC members subjected to blast loading. *Engineering Failure Analysis*, 92:350–367, 2018.
- [19] T. Krauthammer, N. Bazeos, and T.J. Holmquist. Modified SDOF analysis of RC box-type structures. *Journal of Structural Engineering*, 112(4):726–744, 1986.
- [20] M. Nagata, M. Beppu, H. Ichino, and J. Takahashi. Method for evaluating the displacement response of RC beams subjected to close-in explosion using modified SDOF model. *Engineering Structures*, 157:105–118, 2018.
- [21] L. Mao, S.J. Barnett, A. Tyas, J. Warren, G.K. Schleyer, and S.S. Zaini. Response of small scale ultra high performance fibre reinforced concrete slabs to blast loading. *Construction and building materials*, 93:822–830, 2015.
- [22] P.F. Silva and B. Lu. Blast Resistance Capacity of Reinforced Concrete Slabs. *Journal of Structural Engineering*, 135(6):708–716, 2009.
- [23] S. Yao, D. Zhang, X. Chen, F. Lu, and W. Wang. Experimental and numerical study on the dynamic response of RC slabs under blast loading. *Engineering Failure Analysis*, 66:120–129, 2016.
- [24] M. Kristoffersen, A. Minoretti, and T. Børvik. Submerged floating tunnels subjected to internal blast loading. *Proceedings of 7th Transport Research Arena TRA 2018, Vienna, Austria*, 2018. Paper no. 11360.
- [25] X. Zhao, G. Wang, W. Lu, M. Chen, P. Yan, and C. Zhou. Effects of close proximity underwater explosion on the nonlinear dynamic response of concrete gravity dams with orifices. *Engineering Failure Analysis*, 92:566–586, 2018.

- 635 [26] M. Colombo, P. Martinelli, and M. di Prisco. On the blast resistance of high performance tunnel segments. *Materials and Structures*, 49:117–131, 2016.
- [27] M. Foglar and M. Kovar. Conclusions from experimental testing of blast resistance of FRC and RC bridge decks. *International Journal of Impact Engineering*, 59:18–28, 2013.
- [28] M.R. Shiravand and P. Parvanehro. Numerical study on damage mechanism of post-tensioned concrete box
640 bridges under close-in deck explosion. *Engineering Failure Analysis*, 81:103–116, 2017.
- [29] Y. Pan, C.E. Ventura, and M.M.S. Cheung. Performance of highway bridges subjected to blast loads. *Engineering Structures*, 151:788–801, 2017.
- [30] M. Kristoffersen, K.O. Hauge, and T. Børvik. Blast loading of concrete pipes using C-4 charges. *Proceedings*, 2(8):428, 2018. DOI: 10.3390/ICEM18-05292.
- 645 [31] R.K. Chaudhary, S. Mishra, T. Chakraborty, and V. Matsagar. Vulnerability analysis of tunnel linings under blast loading. *International Journal of Protective Structures*, 10(1):73–94, 2019.
- [32] *ABAQUS analysis user’s manual version 2019*. SIMULIA, 2018.
- [33] V. Aune, E. Fagerholt, M. Langseth, and T. Børvik. A shock tube facility to generate blast loading on structures. *International Journal of Protective Structures*, 7:340–366, 2016.
- 650 [34] M. Kristoffersen, J.E. Pettersen, V. Aune, and T. Børvik. Experimental and numerical studies of the structural response of normal strength concrete slabs subjected to blast loading. *Engineering Structures*, 174:242–255, 2018.
- [35] F. Toutlemonde, P. Rossi, C. Boulay, C. Gourraud, and D. Guedon. Dynamic behaviour of concrete: tests of slabs with a shock tube. *Materials and Structures*, 28:293–298, 1995.
- 655 [36] Y. Li, O. Algassem, and H. Aoude. Response of high-strength reinforced concrete beams under shock-tube induced blast loading. *Construction and building materials*, 189:420–437, 2018.
- [37] E. Fagerholt. User manual eCorr – Digital Image Correlation tool. 2019. <https://www.ntnu.edu/kt/ecorr> Accessed 29.04.2019.
- [38] M. Kristoffersen, M. Langseth, and T. Børvik. Combined three-point bending and axial tension of pressurised
660 and unpressurised X65 offshore steel pipes – Experiments and simulations. *Marine Structures*, 61:560–577, 2018.
- [39] M. Eidem, A. Minoretti, and J.H. Sekse. Proposal for a submerged floating tube bridge as part of the Bømlafjord crossing. *19th Congress of the International Association for Bridge and Structural Engineering, Stockholm, Sweden*, 2016. Paper no. Stock-0470-2016-R1.
- [40] C.N. Kingery and G. Bulmash. Airblast parameters from TNT spherical air burst and hemispherical sur-
665 face burst. Technical report, Aberdeen Proving Ground, MD: Defence Technical Information Center, Ballistic Research Laboratory, 1984.
- [41] *NS-EN 1992-1-1: Design of concrete structures – Part 1-1: General rules and rules for buildings*. Standard Norge, 2004.
- [42] R.G. Patel, D.C. Killoh, L.J. Parrott, and W.A. Gutteridge. Influence of curing at different relative humidities
670 upon compound reactions and porosity in Portland cement paste. *Materials and Structures*, 21:192–197, 1988.
- [43] J.R. del Viso, J.R. Carmona, and G. Ruiz. Shape and size effects on the compressive strength of high-strength concrete. *Cement and Concrete Research*, 38:386–395, 2008.

- [44] A.J. Hamad. Size and shape effect of specimen on the compressive strength of HPLWFC reinforced with glass fibres. *Journal of King Saud University - Engineering Sciences*, 29(4):373–380, 2017.
- 675 [45] J. Lubliner, J. Oliver, S. Oller, and E. Oñate. A plastic-damage model for concrete. *International Journal of Solids and Structures*, 25:299–326, 1989.
- [46] J. Lee and G.L. Fenves. Plastic-damage model for cyclic loading of concrete structures. *Journal of Engineering Mechanics*, 124:892–900, 1998.
- [47] P. Baltay and A. Gjelsvik. Coefficient of Friction for Steel on Concrete at High Normal Stresses. *Journal of*
680 *Materials in Civil Engineering*, 2:46–49, 1990.
- [48] T. Jankowiak and T. Lodygowski. Identification of parameters of concrete damage plasticity constitutive model. *Foundations of Civil and Environmental Engineering*, 6:53–69, 2005.
- [49] Comité Euro-International du Béton. *CEB-FIP Model Code 1990*. Thomas Telford Services Ltd, 1993. ISBN 0-7277-1696-4.
- 685 [50] G.R. Johnson and W.H. Cook. A constitutive model and data for metals subjected to large strains, high strain rates and high temperatures. *Proceedings of the 7th International Symposium on Ballistics*, pages 541–547, 1983.
- [51] T. Børvik, M. Langseth, O.S. Hopperstad, and K.A. Malo. Ballistic penetration of steel plates. *International Journal of Impact Engineering*, 22:855–886, 1999.
- [52] M. Kristoffersen, F. Casadei, T. Børvik, M. Langseth, and O.S. Hopperstad. Impact against empty and water-
690 filled X65 steel pipes – Experiments and simulations. *International Journal of Impact Engineering*, 71:73–88, 2014.
- [53] V. Aune, G. Valsamos, F. Casadei, M. Larcher, M. Langseth, and T. Børvik. Use of damage-based mesh adaptivity to predict ductile failure in blast-loaded aluminium plates. *Procedia Engineering*, 197:3–12, 2017.
- [54] M. Kristoffersen, K. Osnes, S.R. Haug, V. Aune, and T. Børvik. Shock tube testing and numerical simulations
695 of concrete slabs. *1st International Conference on Impact Loading of Structures and Materials*, Turin, Italy, 2016.
- [55] P. Rossi and X. Wu. Probabilistic model for material behaviour analysis and appraisalment of concrete structures. *Magazine of Concrete Research*, 44:271–280, 1992.
- [56] A. Antoniou, L. Daudeville, P. Marin, A. Omar, and S. Potapov. Discrete element modelling of concrete
700 structures under hard impact by ogive-node steel projectiles. *European Physical Journal – Special Topics*, 227:143–154, 2018.
- [57] X. Zhou and H. Hao. Mesoscale modelling of concrete tensile failure mechanism at high strain rates. *Computers and Structures*, 86:2013–2026, 2008.
- [58] L. Skorpa. Developing new methods to cross wide and deep Norwegian fjords. *Procedia Engineering*, 4:81–89,
705 2010.
- [59] F.G. Friedlander. The diffraction of sound pulses I: Diffraction by a semi-infinite plane. *Proceedings of the Royal Society A: Mathematical, physical and engineering sciences*, (1006):322–344, 1946.
- [60] J. Shin, A.S. Whittaker, and D. Cormie. Incident and normally reflected overpressure and impulse for detonations of spherical high explosives in free air. *Journal of Structural Engineering*, 141(12), 2015.
710 DOI: 10.1061/(ASCE)ST.1943-541X.0001305.

- [61] S.E. Rigby, A. Tyas, S.D. Clarke, S.D. Fay, J.J. Reay, J.A. Warren, M. Gant, and I. Elgy. Observations from preliminary experiments on spatial and temporal pressure measurements from near-field free air explosions. *International Journal of Protective Structures*, 6:175–190, 2015.
- [62] I. Barsoum, S.A. Lawal, R.J. Simmons, and C.C. Rodrigues. Failure analysis of a pressure vessel subjected to an internal blast load. *Engineering Failure Analysis*, 91:354–369, 2018.
- 715 [63] T. Krauthammer. *Modern Protective Structures*. CRC Press, Taylor and Francis Group, 2008. ISBN 0-8247-2526-3.
- [64] A. Tyas, J.J. Reay, S.D. Fay, S.D. Clarke, S.E. Rigby, J.A. Warren, and D.J. Pope. Experimental studies of the effect of rapid afterburn on shock development of near-field explosions. *International Journal of Protective Structures*, 7(3):452–465, 2016.
- 720 [65] I.E. Edri, H.Y. Grisaro, and D.Z. Yankelevsky. TNT equivalency in an internal explosion event. *Journal of Hazardous Materials*, 374:248–257, 2019.
- [66] M. Larcher and F. Casadei. Explosions in complex geometries – A comparison of several approaches. *International Journal of Protective Structures*, 1:169–195, 2010.
- 725 [67] T. Børvik, A.G. Hanssen, M. Langseth, and L. Olovsson. Response of structures to planar blast loads – A finite element engineering approach. *Computers and Structures*, 87:507–520, 2009.
- [68] M.J. Mullin and B.J. O’Toole. Simulation of energy absorbing materials in blast loaded structures. *8th International LS-DYNA Users Conference*, 2004.
- [69] F. Casadei and S. Potapov. Permanent fluid-structure interaction with non-conforming interfaces in fast transient dynamics. *Computer Methods in Applied Mechanics and Engineering*, 193:4157–4194, 2004.
- 730 [70] M. Kristoffersen, K.O. Hauge, G. Valsamos, and T. Børvik. Blast loading of concrete pipes using spherical centrally placed C-4 charges. *European Physical Journal – Web of Conferences*, 183:01057, 2018. DOI: 10.1051/epj-conf/201818301057.
- [71] C.P. Pantelides, T.T. Garfield, W.D. Richins, T.K. Larson, and J.E. Blakeley. Reinforced concrete and fiber reinforced concrete panels subjected to blast detonations and post-blast static tests. *Engineering Structures*, 76:24–33, 2014.
- 735 [72] W. Van Paepegem, S. Palanivelu, J. Degrieck, J. Vantomme, B. Reymen, D. Kakogiannis, D. Van Hemelrijck, and J. Wastiels. Blast performance of a sacrificial cladding with composite tubes for protection of civil engineering structures. *Composites: Part B*, 65:131–146, 2014.
- [73] T. Chakraborty, M. Larcher, and N. Gebekken. Performance of tunnel lining materials under internal blast loading. *International Journal of Protective Structures*, 5(1):83–96, 2014.
- 740 [74] R. Codina, D. Ambrosini, and F. de Borbón. Alternatives to prevent the failure of RC members under close-in blast loadings. *Engineering Failure Analysis*, 60:96–106, 2016.